Custodial vector model

Diego Becciolini,[1,2] Diogo Buarque Franzosi,[1] Roshan Foadi,[3,4] Mads T. Frandsen,[1]
Tuomas Hapola,[5] and Francesco Sannino[1]

[1]*CP³-Origins and the Danish Institute for Advanced Study, University of Southern Denmark,*
Campusvej 55, DK-5230 Odense M, Denmark
[2]*INFN, Sezione di Firenze, Via G. Sansone, 1; I-50019 Sesto Fiorentino, Italy*
[3]*Department of Physics, University of Jyväskylä, P.O. Box 35, Jyväskylä FI-40014, Finland*
[4]*Department of Physics and Helsinki Institute of Physics, University of Helsinki,*
P.O. Box 64, Helsinki FI-000140, Finland
[5]*Institute for Particle Physics Phenomenology, Durham University,*
South Road, Durham DH1 3LE, United Kingdom

We analyze the Large Hadron Collider (LHC) phenomenology of heavy vector resonances with a $SU(2)_L \times SU(2)_R$ spectral global symmetry. This symmetry partially protects the electroweak S parameter from large contributions of the vector resonances. The resulting custodial vector model spectrum and interactions with the standard model fields lead to distinct signatures at the LHC in the diboson, dilepton, and associated Higgs channels.

I. INTRODUCTION

The discovery of the Higgs-like particle at the LHC further supports the remarkable success of the Glashow, Salam, and Weinberg (GSW) theory of electroweak interactions.

The GSW theory augmented with quantum chromodynamics (QCD) is known as the standard model of particle interactions (SM). Any extension of the SM must closely reproduce the GSW theory, including the Higgs sector. It is therefore natural to explore extensions where the low energy effective GSW theory is partially protected against contributions from new sectors via the presence of additional symmetries.

One may either consider perturbative or nonperturbative extensions of the GSW theory. Here we consider the possibility that the new extension features massive spin-1 resonances in the TeV region. This is, for example, expected in any model of composite dynamics near the electroweak scale while many perturbative extensions also feature, via new Higgs mechanisms, massive spin-1 states, e.g., so-called Z' states.

Our model respects the custodial symmetry of the GSW theory, i.e., $G = SU(2)_L \times SU(2)_R$ that protects the mass relation between the electroweak W and Z bosons. It features an additional unbroken global $G' = SU(2)'_L \times SU(2)'_R$ symmetry acting on the heavy spin-1 resonances. The effective Lagrangian thus features two global symmetries G and G'. The former breaks to $H = SU(2)_V$ and the latter remains intact. The breaking $G \to H$ is identified with the GSW custodial symmetry breaking pattern $SU(2)_L \times SU(2)_R \to SU(2)_V$ while G' acts only on the new heavy vector resonances and serves to protect the S parameter as well as longitudinal WW scattering from large contributions from the heavy resonances.

We model the Higgs sector as in the GSW theory. By construction, our model then has the GSW theory as a well-defined decoupling limit when sending the mass of the new resonances to infinity. We shall call our model the custodial vector model (CVM).

A discussion of possible strong dynamics underlying the CVM are given in [1–3]. The spectral symmetry of the vector resonances in the CVM was discussed in [4] and built into the so-called degenerate breaking electroweak symmetry strongly (D-BESS) model [5] without featuring a Higgs particle. The CVM can also be interpreted as an extension of the GWS theory with multiple scalars, in which the massive spin-one bosons arise from new gauge sectors; see e.g., [6–9].

In this paper we introduce the CVM and investigate its LHC phenomenology. The model features a very distinct pattern of narrow spin-1 resonances in the diboson, dilepton, and associated Higgs search channels allowing, in principle, to pin it down. Specifically the CVM predicts closely spaced spin-1 resonance double peaks in the dilepton invariant mass distributions, single resonance peaks in the single charged lepton channels, and suppressed peaks or no signal in the diboson channels. This is in contrast to general effective descriptions of composite dynamics leading to broad, well-spaced resonances with large branching ratios to diboson channels, e.g., [10–13], or to specific spin-1 spectra appearing in composite Higgs models and extra-dimensional theories; see e.g., [14–16].

Higgs production in association with vector bosons is also an important search channel, which depending on the parameter space can be substantially enhanced with respect to the GSW theory.

The outline of the paper is as follows. In Sec. II we discuss current LHC constraints on spin-1 resonances. The CVM Lagrangian is discussed in Sec. III. Here we also outline the qualitative phenomenology. We compare the model predictions with the electroweak precision measurements in Sec. IV. The detailed phenomenological analysis is provided in Sec. V. Finally in Sec. VI we summarize our findings and discuss further developments.

II. CURRENT CONSTRAINTS ON GENERIC VECTOR RESONANCES

Several studies have been dedicated to the LHC phenomenology of heavy spin-1 particles; see for instance [17] for a recent discussion. Here, we focus on the latest experimental results to summarize the relevant LHC searches for vector resonances that will be used to constrain the CVM parameter space in Sec. III.

We consider a set of narrow charged and neutral spin-one resonances, $\mathcal{R}_i^\pm$ and $\mathcal{R}_i^0$, respectively, with i counting the number of independent mass eigenstates. With H we denote the 125 GeV Higgs-like particle. The relevant effective interaction vertices are summarized via contact operators in the Lagrangian:

FIG. 1 (color online). ATLAS and CMS 95% C.L. exclusion limits on production cross section times branching ratio, $\sigma \times$ BR, for a new neutral or charged vector resonance. The charged vector final states are $\ell\nu$, WZ, and WH. Data references are given in Table I.

$$\mathcal{L}^\mathcal{R} = \mathcal{L}_{\text{kinetic}}^\mathcal{R} + \mathcal{L}_{\text{self}}^\mathcal{R} + \mathcal{L}_{\text{fermion}}^\mathcal{R} + \mathcal{L}_{\text{gauge}}^\mathcal{R} + \mathcal{L}_H^\mathcal{R}. \quad (1)$$

The vertices linking the spin-one resonances with the SM fermions are

$$\mathcal{L}_{\text{fermion}}^\mathcal{R} = \sum_i \sum_{u,d} \bar{u} \mathcal{R}_i^+ (g_{\mathcal{R}_i ud}^L P_L + g_{\mathcal{R}_i ud}^R P_R)d + \text{H.c.} + \sum_i \sum_f \bar{f} \mathcal{R}_i^0 (g_{\mathcal{R}_i f}^L P_L + g_{\mathcal{R}_i f}^R P_R)f$$

$$= \sum_i \sum_{u,d} \bar{u} \mathcal{R}_i^+ (g_{\mathcal{R}_i ud}^V - g_{\mathcal{R}_i ud}^A \gamma_5)d + \text{H.c.} + \sum_i \sum_f \bar{f} \mathcal{R}_i^0 (g_{\mathcal{R}_i f}^V - g_{\mathcal{R}_i f}^A \gamma_5)f, \quad (2)$$

where u (d) runs over all up-type (down-type) quarks and leptons, f runs over all quark and lepton flavors, and we have expressed the vertices both in left-right and vector-axial basis, with $P_{L/R} = (1 \pm \gamma_5)/2$.

The CP-invariant trilinear interactions of the spin-one resonances with H are

$$\mathcal{L}_H^\mathcal{R} \supset \sum_i g_{\mathcal{R}_i ZH} \mathcal{R}_{i\mu}^0 Z^\mu H + g_{\mathcal{R}_i WH}(\mathcal{R}_{i\mu}^+ W^{-\mu} + \mathcal{R}_{i\mu}^- W^{+\mu})H$$

$$+ \frac{1}{2}\sum_{i,j} g_{\mathcal{R}_i^0 \mathcal{R}_j^0 H} \mathcal{R}_{i\mu}^0 \mathcal{R}_j^{0\mu} H + g_{\mathcal{R}_i^+ \mathcal{R}_j^- H} \mathcal{R}_{i\mu}^+ \mathcal{R}_j^{-\mu} H. \quad (3)$$

Note that a vertex with one spin-one resonance and two scalars H is not CP invariant, and is therefore not included in $\mathcal{L}_H^R$ [18].

For single resonance production and subsequent decay, in $\mathcal{L}_{\text{gauge}}^R$ we only need to consider the vertices with one resonance and two SM gauge bosons, as triboson final states are suppressed compared to the diboson ones, due to smaller available phase space. The C- and P-invariant interactions are
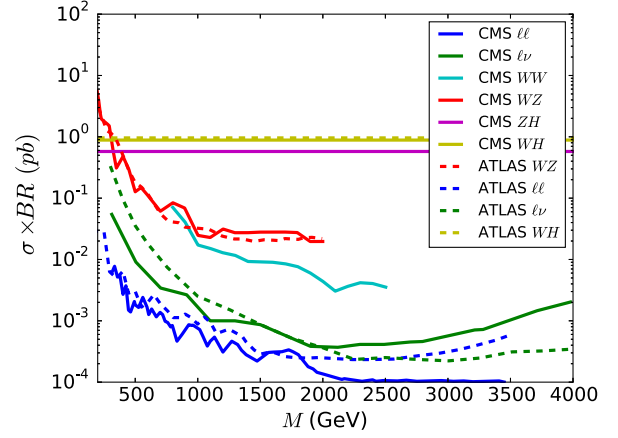
$$\mathcal{L}_{\text{gauge}}^\mathcal{R} \supset \sum_i [g_{\mathcal{R}_i WW}^{(1)}[[W^+ W^- \mathcal{R}_i^0]] + g_{\mathcal{R}_i WW}^{(2)}[[\mathcal{R}_i^0 W^+ W^-]]$$

$$+ g_{\mathcal{R}_i WZ}^{(1)}(\mathcal{R}_{i\mu\nu}^+ W^{-\nu} - \mathcal{R}_{i\mu\nu}^- W^{+\nu} + W_{\mu\nu}^+ \mathcal{R}_i^{-\nu}$$

$$- W_{\mu\nu}^- \mathcal{R}_i^{+\nu})Z^\mu + g_{\mathcal{R}_i WZ}^{(2)}(\mathcal{R}_{i\mu}^+ W^{-\nu} - \mathcal{R}_{i\mu}^- W^{+\nu})Z^{\mu\nu}] \quad (4)$$

where

$$[[V_1 V_2 V_3]] \equiv i\partial_\mu V_{1\nu} V_2^{[\mu} V_3^{\nu]} + \text{H.c.},$$

$$\mathcal{R}_{\mu\nu} \equiv \partial_\mu \mathcal{R}_\nu - \partial_\nu \mathcal{R}_\mu. \quad (5)$$

The 2-body decay modes of $\mathcal{R}_i^\pm$ and $\mathcal{R}_i^0$ may be then summarized as

$$\Gamma_{\mathcal{R}_i^\pm} = \sum_{u,d} \Gamma_{\mathcal{R}_i^\pm}^{ud} + \sum_{\nu,e} \Gamma_{\mathcal{R}_i^\pm}^{\nu e} + \Gamma_{\mathcal{R}_i^\pm}^{WZ} + \Gamma_{\mathcal{R}_i^\pm}^{WH},$$

$$\Gamma_{\mathcal{R}_i^0} = \sum_q \Gamma_{\mathcal{R}_i^0}^{q\bar{q}} + \sum_\ell \Gamma_{\mathcal{R}_i^0}^{\ell\bar{\ell}} + \sum_\nu \Gamma_{\mathcal{R}_i^0}^{\nu\bar{\nu}} + \Gamma_{\mathcal{R}_i^0}^{WW} + \Gamma_{\mathcal{R}_i^0}^{ZH}, \quad (6)$$

TABLE I.   LHC searches used to constrain the CVM.

Channel [Exp]	L [fb^{-1}]	Mass range [GeV]	Reference
$pp \to \ell^+ \ell^-$ [CMS]	20.6 (8 TeV)	300–2500	[19]
$pp \to \ell^+ \ell^-$ [ATLAS]	20.3 (8 TeV)	200–3000	[20]
$pp \to WZ$ [a][ATLAS]	20.3 (8 TeV)	200–2000	[21]
$pp \to WZ$[b] [CMS]	19.6 (8 TeV)	200–2000	[22]
$pp \to WW$[c] [ATLAS]	4.7 (7 TeV)	200–1500	[23]
$pp \to WW$ [CMS]	19.7 (8 TeV)	800–2500	[24]
$pp \to Z/WH$ [CMS]	18.9 (8 TeV)	*	[25]
$pp \to WH$[d] [ATLAS]	20.3 (8 TeV)	*	[26]
$pp \to \ell\nu$ [CMS]	20	300–4000	[27]
$pp \to \ell\nu$ [ATLAS]	20.3	300–4000	[28]

[a]Fully leptonic analysis, see [29] for similar limits from a semileptonic analysis.
[b]Semileptonic analysis, see [30] for a boosted semileptonic analysis.
[c]Not shown in Fig. 1 due to the low luminosity.
[d]The ZH analysis of ATLAS is not relevant as explained in Sec. V C.

where the formulas for the partial widths are provided in Appendix C. We disregard the subdominant 3- and 4-body decay modes.

The relevant current LHC limits for a single charged or neutral vector resonance are given in Fig. 1 and the corresponding data listed in Table I. The dilepton limits are at least an order of magnitude stronger than any of the diboson limits at any resonance mass.

The ATLAS dilepton limit on the figure is the one relevant for a sequential standard model (SSM) Z' in [20]. The CMS limits on the $\ell^+\ell^-$ production [19] are expressed in terms of $R_\sigma \equiv \frac{\sigma(pp \to Z' + X \to \ell\ell + X)}{\sigma(pp \to Z + X \to \ell\ell + X)}$. We convert the bounds on R_σ to bounds on the total inclusive cross section. We use the total standard model cross section for the Drell Yan Z boson production given in [31]. Similarly, for the associated Higgs production, the limits in [25] are given in terms of the signal strength, $\mu \equiv \sigma/\sigma_{\rm SM}$. We convert this to a limit on the cross section, $\sigma_{\rm BSM} = \sigma - \sigma_{\rm SM}$. For $\sigma_{\rm SM}$ we use the prediction at NNLO QCD and NLO electroweak accuracy [32]. The WZ channel CMS search gives exclusion for the fully decayed three leptons and missing energy final state; therefore, we obtain the limit on the WZ cross section by correcting for the W and Z branching ratios.

III. THE CUSTODIAL VECTOR MODEL

The CVM, like the GSW theory, possesses a global $SU(2)_L \times SU(2)_R$ chiral symmetry which breaks spontaneously to the diagonal $SU(2)_V$ symmetry. It is well known that this custodial symmetry protects the T parameter. The electroweak gauge symmetry group $SU(2)_L \times U(1)_Y$ is embedded in $SU(2)_L \times SU(2)_R$ and therefore provides a small breaking of the custodial symmetry. Upon spontaneous symmetry breaking the final intact gauge symmetry is $U(1)_{\rm QED}$.

The CVM features the Higgs state H and two weak isospin triplet vector resonances. The GSW custodial symmetry is encoded in the Higgs Lagrangian and the model includes yet another custodial symmetry acting on the vector sector. The new custodial symmetry is simply $SU(2)'_L \times SU(2)'_R$ and protects the S parameter and WW scattering from large corrections coming from the vector sector [2–5,33–35], as we shall show below.

To elucidate the patterns of chiral symmetry breaking we use a linear representation of the original chiral symmetry group, both for the Higgs and vector sector. The Higgs H and the electroweak Goldstone bosons Π^a constitute a weak doublet that can be represented via

$$\Sigma = \frac{1}{\sqrt{2}}[v + H + 2i\Pi^a T^a], \qquad (7)$$

where $T^a = \tau^a/2$ with τ^a the Pauli matrices. Here v is the vacuum expectation value (VEV) and Σ transforms as a bifundamental of the chiral symmetry group:

$$\Sigma \to u_L \Sigma u_R^\dagger, \qquad u_{L/R} \in SU(2)_{L/R}. \qquad (8)$$

The electroweak gauge boson interactions with Σ are introduced via the covariant derivative

$$D_\mu \Sigma = \partial_\mu \Sigma - ig\tilde{W}_\mu^a T^a \Sigma + ig'\Sigma\tilde{B}_\mu T^3, \qquad (9)$$

where the tildes over the gauge fields indicate that these are not yet mass eigenstates. The new heavy vectors, $A_L \equiv A_L^a T^a$ and $A_R \equiv A_R^a T^a$, are formally introduced, following [2], as gauge fields transforming under the original chiral symmetry group, i.e.,

$$A_{L/R}^\mu \to u_{L/R}\left(A_{L/R}^\mu + \frac{i}{g}\partial^\mu\right)u_{L/R}^\dagger, \qquad u_{L/R} \in SU(2)_{L/R}, \qquad (10)$$

where $\tilde{g}$ is the self-coupling. Note that we have used a single coupling for both A_L and A_R: in fact we assume that the new CVM sector is invariant under parity, i.e.,

$$\Sigma(t,\vec{x}) \leftrightarrow \Sigma^\dagger(t,-\vec{x}), \qquad A_L(t,\vec{x}) \leftrightarrow A_R(t,-\vec{x}). \tag{11}$$

The linear combinations [2]

$$C_{L\mu} \equiv A_{L\mu} - \frac{g}{\tilde{g}}\tilde{W}_\mu, \qquad C_{R\mu} \equiv A_{R\mu} - \frac{g'}{\tilde{g}}\tilde{B}_\mu, \tag{12}$$

transform homogeneously under the electroweak subgroup and can be immediately used to build Lagrangian invariants. As shown in [2] the following Lagrangian

$$\begin{aligned}
\mathcal{L}_{\text{boson}} = &-\frac{1}{2}\text{Tr}[\tilde{W}_{\mu\nu}\tilde{W}^{\mu\nu}] - \frac{1}{4}\tilde{B}_{\mu\nu}\tilde{B}^{\mu\nu} - \frac{1}{2}\text{Tr}[F_{L\mu\nu}F_L^{\mu\nu} + F_{R\mu\nu}F_R^{\mu\nu}] \\
&+ \frac{1}{2}\text{Tr}[D_\mu\Sigma D^\mu\Sigma^\dagger] + \frac{\tilde{g}^2 f^2}{4}\text{Tr}[C_{L\mu}^2 + C_{R\mu}^2] + \frac{\tilde{g}^2 s}{4}\text{Tr}[C_{L\mu}^2 + C_{R\mu}^2]\text{Tr}[\Sigma\Sigma^\dagger] \\
&+ \frac{\mu^2}{2}\text{Tr}[\Sigma\Sigma^\dagger] - \frac{\lambda}{4}\text{Tr}[\Sigma\Sigma^\dagger]^2
\end{aligned} \tag{13}$$

preserves $SU(2)_L \times SU(2)_R \times SU(2)_L' \times SU(2)_R'$ when the electroweak gauge interactions are switched off. It is straightforward to see that in this limit the vectors can be transformed independently as

$$A_{L/R} \to u_{L/R}' A_{L/R} u_{L/R}'^\dagger, \qquad u_{L/R}' \in SU(2)_{L/R}'. \tag{14}$$

Adding an $SU(2)_L \times SU(2)_R$-invariant term like $\text{Tr}[C_{L\mu}(\Sigma D^\mu\Sigma^\dagger - D^\mu\Sigma\Sigma^\dagger)] + (L \leftrightarrow R)$ would break the $SU(2)_L' \times SU(2)_R'$ symmetry and contribute to the electroweak S parameter as computed in e.g., [10].

In the Lagrangian $\tilde{W}_{\mu\nu}$ and $\tilde{B}_{\mu\nu}$ are the ordinary electroweak field strength tensors, whereas $F_{L\mu\nu}$ and $F_{R\mu\nu}$ are the field-strength tensors built out of the spin-one fields A_L and A_R, respectively. The coupling s is real and f is a new mass scale for the heavy vectors.

Because μ^2 is positive, Σ acquires a VEV, given at tree level by

$$v = \mu/\sqrt{\lambda}. \tag{15}$$

Upon diagonalizing the mass matrices we end up with the ordinary GSW gauge bosons, and two nearly mass-degenerate triplets of heavy vectors. The physical heavy vectors are denoted by $L^{\pm,0}$ and $R^{\pm,0}$. They are dominantly A_L and A_R, respectively. In Appendixes A, B, and C we diagonalize the mass matrices and evaluate the couplings and widths of the spin-one resonances.

It is useful to sketch the basic qualitative features of the CVM phenomenology before the quantitative study presented in Sec. V. The new $SU(2)_L' \times SU(2)_R'$ custodial symmetry over the vectors has an immediate impact on the partial decay widths of the vectors into either fermions or bosons, which scale as

$$\Gamma_{\mathcal{R}_i}^{\bar{f}f'} \sim \Gamma_{\mathcal{R}_i}^{VV'} \sim \frac{1}{a}\Gamma_{\mathcal{R}_i}^{HV} \sim \frac{M_R}{\tilde{g}^2}, \tag{16}$$

where

$$M_R^2 \equiv \frac{\tilde{g}^2}{4}(f^2 + sv^2) \tag{17}$$

is the mass of the vectors in the absence of the subdominant electroweak corrections. V, V' denote the W, Z bosons. We also trade the parameter s for the parameter

$$a = \frac{f^2}{f^2 + sv^2} = \frac{\tilde{g}^2 f^2}{4M_R^2}, \tag{18}$$

because it controls the ratio of the partial width $\Gamma_{\mathcal{R}_i}^{HV}$ to the other partial widths of the model; see (16).

The dominant production mode of the CVM vectors is the Drell-Yan (DY) process. From the partial widths scaling above and from the LHC limits shown in Fig. 1 it follows that for the CVM the strongest constraints arise from the dilepton final state provided a is not much larger than unity. The LHC constraint from the associate Higgs production final states HV is dominant when a is large.[1] We detail this in Sec. V C. a is not expected to be too large either: this would correspond to a situation where M_R, because of a cancellation between f^2 and sv^2, becomes significantly smaller than f (for reasonable values of $\tilde{g}$). For instance if $M_R \sim f$ and $\tilde{g} \sim 10$, then $a \sim 25$; we will not consider values of a larger than this. Typically, a should be of $\mathcal{O}(1)$ while $a = 0$ corresponds to $f = 0$ and the mass scale of new physics provided by sv^2 alone.

---

[1]Notice a can assume negative values if a negative f^2 is allowed (compensated by a positive sv^2), the interpretation of which, however, is unclear though we still allow it in our analysis; while DY production depends on a only through the Higgs contribution to the CVM vector width, which is proportional to $|a|^2$, associated Higgs production receives contributions proportional to a and $a - 1$.

It is useful to define δ, the fractional difference between the ZZ-Higgs coupling in the CVM with respect to the GSW Higgs, as an alternative to a; a is indeed the parameter directly controlling δ,

$$1 - \delta \equiv \frac{g_{HZZ}}{g_{HZZ}^{SM}} \quad \text{with} \quad g_{HZZ}^{SM} \equiv \frac{2}{v} M_Z^2, \qquad (19)$$

where M_Z is the Z mass, and the sign of δ is chosen such that it coincides with the one of a. From the explicit expression of g_{HZZ} derived in Eq. (B9) we get the approximate expression

$$\delta \simeq a \frac{v^2 (g'^4 + g^4)}{4 \tilde{g}^2 M_R^2} \simeq a \frac{1}{\tilde{g}^2} \left(\frac{55 \text{ GeV}}{M_R} \right)^2, \qquad (20)$$

obtained assuming $M_R \gg M_W$ and $\tilde{g} \gg 1$; note that δ is exactly proportional to a, not only in the limit of large M_R and $\tilde{g}$. On the other hand, the deviation from the GSW relation for the WW-Higgs coupling, δ_W, does not vanish when $a = 0$ because the tree-level W-boson mass is modified in the CVM. The relation is given in Eq. (B10), and is approximately

$$\delta_W \simeq 0.9 \delta - \frac{1}{\tilde{g}^2} \left(\frac{40 \text{ GeV}}{M_R} \right)^2 \simeq (a - 0.6) \frac{1}{\tilde{g}^2} \left(\frac{50 \text{ GeV}}{M_R} \right)^2. \qquad (21)$$

The Yukawa sector of the CVM is modeled after the GSW theory to include minimal flavor violation and consequently minimize tension with experimental results from flavor physics.

Intriguingly the CVM is challenging to uncover at the LHC even for vector masses in the TeV region and not too large values of $\tilde{g}$. The reason being that, for order unity values of all the couplings, the vectors are very narrow and therefore their line shapes are difficult to reconstruct with current experimental resolution. Furthermore for $\tilde{g} \gtrsim 2$ even the spacing in the mass of the two resonances is less than the current experimental resolution in the dilepton invariant masses making it impossible to resolve them.

For sufficiently large values of a the partial width of $R \to HV$ grows and of course the overall width grows too. In this case one can reconstruct the overall line shape but cannot resolve the two closely spaced resonances because they significantly overlap.

We also note that due to the enhanced symmetry over the vectors, the charged right resonances $R^\pm$ are stable. However we expect the CVM symmetry to be only approximate in the full theory. If the breaking is very small the $R^\pm$ are long lived. They are pair produced via a Drell-Yan process and will leave tracks in the CMS tracker and muon system [36]. The exclusion limit shown in Fig. 2 is independent of $\tilde{g}$ and a to leading order and rules out values of M_R below $\simeq 300$ GeV so this constraint is currently weak.
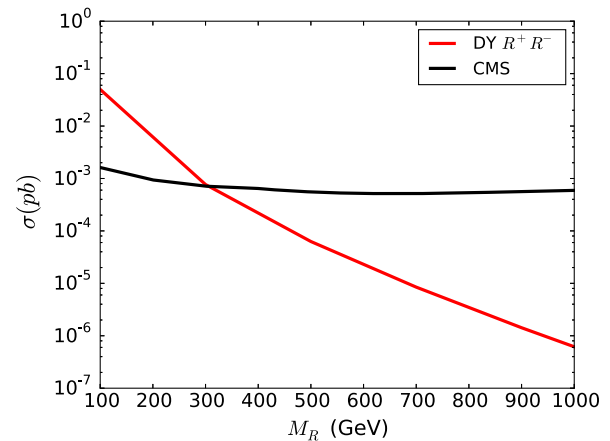

FIG. 2 (color online). Full signal cross section for $R^+ R^-$ pair production at the LHC with $\sqrt{s} = 8$ TeV. The 95% exclusion limit on long-lived charged particles provided by CMS is given in the black curve [36].

IV. ELECTROWEAK PRECISION TESTS

Contributions from the CVM to the electroweak observables are suppressed relative to generic models with vector resonances and scalars for two reasons: the global symmetry acting on the vectors, and the presence of a very SM-like Higgs state. We will now discuss in turn these contributions.

A. Vector sector

The CVM contributions to the electroweak parameters S and T from the heavy vector bosons vanish because of the two custodial symmetries of the model. The vector contribution to the T parameter is zero at tree level because the model respects ordinary custodial symmetry. The contribution to the S parameter stemming from the heavy spin-1 resonances vanishes because the $SU(2)'_L \times SU(2)'_R$ insures parity doubling of the vector spectrum and decay constants. To elucidate this point we observe that the S-parameter contribution from a genetic vector and axial resonance contribution reads

$$S = 4\pi \left[\frac{F_V^2}{M_V^2} - \frac{F_A^2}{M_A^2} \right] \qquad (22)$$

with the expressions for the decay constants and masses given in [10]. The $SU(2)'_L \times SU(2)'_R$ symmetry implies that $F_V = F_A$ and $M_V = M_A$, thus the vector contribution to the S parameter vanishes as discussed further in [2,3,37]. More generally, the electroweak S parameter, after integrating out all heavy vector and scalar states, can be described in the effective Lagrangian by the operator $\text{Tr}[W^{\mu\nu} \Sigma B^{\mu\nu} \Sigma^\dagger]$. Any new contribution, before integrating out heavy vectors, would involve insertion of A_L or A_R but that is not allowed by the $SU(2)'_L \times SU(2)'_R$ symmetry. Note that the discrete $Z'_{2L} \times Z'_{2R}$ symmetry acting as

$A_{L/R} \to z_{L/R}A_{L/R}$, with $z_{L/R} = \pm 1$ is sufficient to ensure the vanishing of the vector contribution to S at tree level.

According to the parametrization of electroweak observables [38], only the custodial and isospin preserving parameters W and Y are now nonvanishing [3,39,40]:

$$W = \frac{4\cos^4\theta M_Z^4}{\tilde{g}^2 v^2 M_R^2}, \qquad Y = \frac{\sin^2(2\theta)M_Z^4}{\tilde{g}^2 v^2 M_R^2}. \qquad (23)$$

B. Higgs sector

The presence of a light SM-like scalar—now experimentally established—provides important corrections to electroweak observables for a good agreement with data, such that effects from new physics need only be small rather than having to mimic a Higgs boson. While the contributions from the spin-1 resonances in our model are under control thanks to the custodial symmetry, we do allow a small misalignment between the vector-boson-mass matrix and the scalar-coupling matrix, parametrized by a [or equivalently δ (20)]. This implies a deviation in the couplings of the Higgs boson to the electroweak bosons in the CVM and thus contributions to S and T. These have previously been determined in full in [41]. We will however conclude that this additional effect is even less important than the spin-1 contributions.

Approximate expressions of the contributions to the electroweak parameters read

$$\hat{S} \approx \delta \frac{\alpha}{12\pi\sin^2\theta}\ln\frac{\Lambda}{M_h}, \qquad \hat{T} \approx -\delta\frac{3\alpha}{4\pi\cos^2\theta}\ln\frac{\Lambda}{M_h}, \qquad \hat{U} \approx 0, \qquad (24)$$

where M_h is the Higgs mass, α is the electromagnetic coupling at the Z pole and θ the Weinberg angle defined as

$$\sin^2 2\theta \equiv \frac{4\pi\alpha}{\sqrt{2}G_F M_Z^2} = \frac{e^2 v^2}{M_Z^2}. \qquad (25)$$

To provide simple constraints on δ we approximate here the renormalization procedure [41] by the presence of a physical cutoff Λ which is expected to be around the
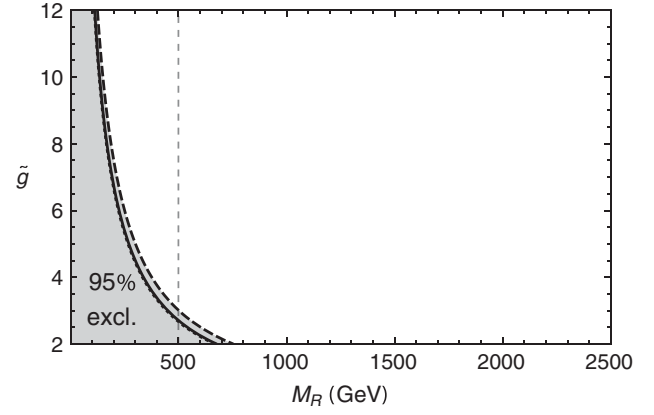

FIG. 3. Exclusion limits at 95% C.L. in the $(M_R, \tilde{g})$ plane from electroweak precision measurements on the CVM vector resonances. Dotted, continuous, and dashed lines for $a = 25$, 0, and -25, respectively. The vertical separation line is meant to guide the eye: plots at the end of the paper only start at $M_R = 500$ GeV.

new resonances mass scale, i.e., $4\pi v$. Ignoring for an instant the contributions from the vector resonances, we deduce the following approximate bounds on δ at 95% C.L.—adapting the analysis in [42,43]:

$$-0.09 < \delta < 0.03. \qquad (26)$$

The limits are comparable to the ones from the direct Higgs couplings measurements [44] that at two-sigmas yield,

$$-0.31 < \delta < 0.01. \qquad (27)$$

C. Limits

The effect on electroweak observables is best expressed in terms of the ϵ parameters [45], and one has [with (23)–(24) and $V = X = 0$] [38]:

$$\delta\epsilon_1 = \hat{T} - W - \tan^2\theta Y, \quad \delta\epsilon_2 = \hat{U} - W, \quad \delta\epsilon_3 = \hat{S} - W - Y. \qquad (28)$$

A recent fit from [43] gives

$$
\begin{aligned}
10^3\delta\epsilon_1 &= 0.7 \pm 1.0 \\
10^3\delta\epsilon_2 &= -0.1 \pm 0.9 \quad \text{with correlation matrix } \rho = \begin{pmatrix} 1 & 0.80 & 0.86 \\ 0.80 & 1 & 0.51 \\ 0.86 & 0.51 & 1 \end{pmatrix}, \\
10^3\delta\epsilon_3 &= 0.6 \pm 0.9
\end{aligned} \qquad (29)
$$

and performing a simple χ^2 test, we obtain the exclusion limits on $(M_R, \tilde{g})$, shown in Fig. 3, adding the Higgs contributions above for fixed values of a and δ given by (20). Even for the extreme values $|a| = 25$, at the edge of

the parameter space we will be considering, the dominant effect is the one from the vector resonances.

However, due to the double suppression—in $\tilde{g}^{-2}$ and M_R^{-2}—of the new physics contributions to W and Y,
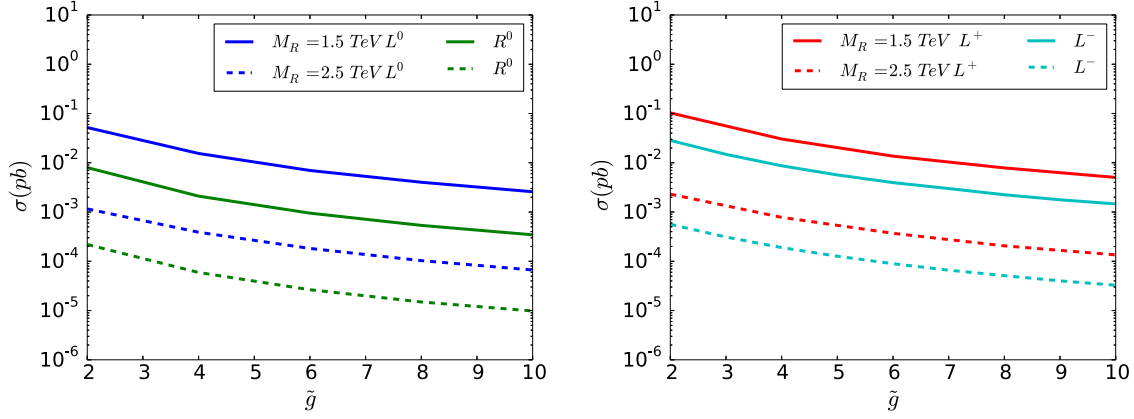
FIG. 4 (color online). LHC production cross section of the heavy CVM vector resonances at $\sqrt{s} = 8$ TeV as a function of $\tilde{g}$ for $M_R = 1500$ GeV (solid lines) and $M_R = 2500$ GeV (dashed lines). On the left we show L^0 (blue) and R^0 (green). On the right we show L^+ (red) and L^- (cyan).

electroweak constraints are overall very weak and direct searches for the vector resonances are much more important.

In the low $(\tilde{g}, M_R)$ region of parameter space shown in Fig. 3, direct measurements of the Higgs boson couplings can be competitive with electroweak precision test for extreme values of a. The δ parameter measuring the Higgs coupling deviations from their SM values can reach the percent level here. In this region the difference between W and Z boson couplings to the Higgs boson could also be experimentally accessed. In practice, however, direct searches for the vector resonances are much more constraining and rule out this parameter region, as we are going to see in the next section.

V. LHC PHENOMENOLOGY

In this section we present the detailed LHC phenomenology of the CVM, previously sketched in Sec. III. To aide numerical computations, the model is implemented in MADGRAPH 5 [46] using the FEYNRULES package [47]. In our computations we use the following electroweak parameters:

$$M_Z = 91.2 \text{ GeV},$$
$$G_F = 1.16637 \times 10^{-5} \text{ GeV}^{-2},$$
$$\alpha^{-1}(M_Z) = 127.9,$$
$$M_t = 172 \text{ GeV}. \tag{30}$$

In addition to these, the CVM is parametrized by the three parameters, characterizing the new spin-one resonances

$$M_R, \qquad \tilde{g}, \qquad a, \tag{31}$$

where M_R is the mass scale of the heavy resonances, $\tilde{g}$ is their self-coupling and a was defined in Eq. (18). Instead of

a we will sometimes use δ defined in Eq. (19). Values of δ/a range from $\delta/a \approx 0.000003$–$0.003$ for $(\tilde{g}, M_R)$ between (12, 2500 GeV) and (2, 500 GeV). So unless a is large, the HZZ and HWW couplings are very SM-like in the model.

The LHC production cross sections of the new vector resonances, at $\sqrt{s} = 8$ TeV center-of-mass energy, are shown in Fig. 4 as a function of $\tilde{g}$ for different values of M_R. Due to the factorizable nature of the QCD corrections for the Drell-Yan production, the inclusive cross section at NNLO accuracy in QCD is given by

$$\sigma_{\text{NNLO}} = \sigma_{\text{LO}} \times K, \tag{32}$$

where σ_{LO} is the leading order prediction and the K factor depends only on the mass of the resonance. We use $K = 1.16$ for the neutral vector resonance production and 1.2 for
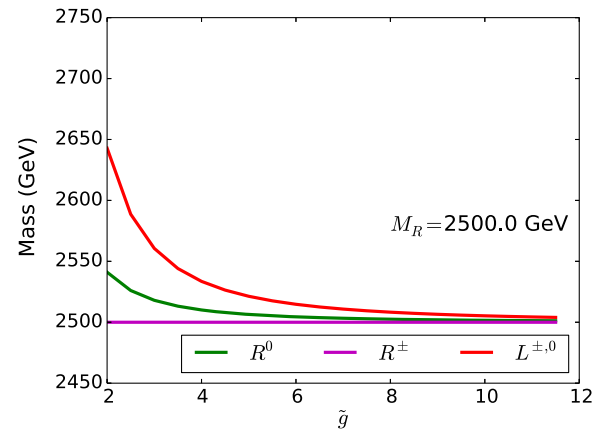

FIG. 5 (color online). Masses of the heavy CVM vector resonances for $M_R = 2500$ GeV. The difference in mass between the charged and neutral L states is negligible and cannot be seen on the plot.
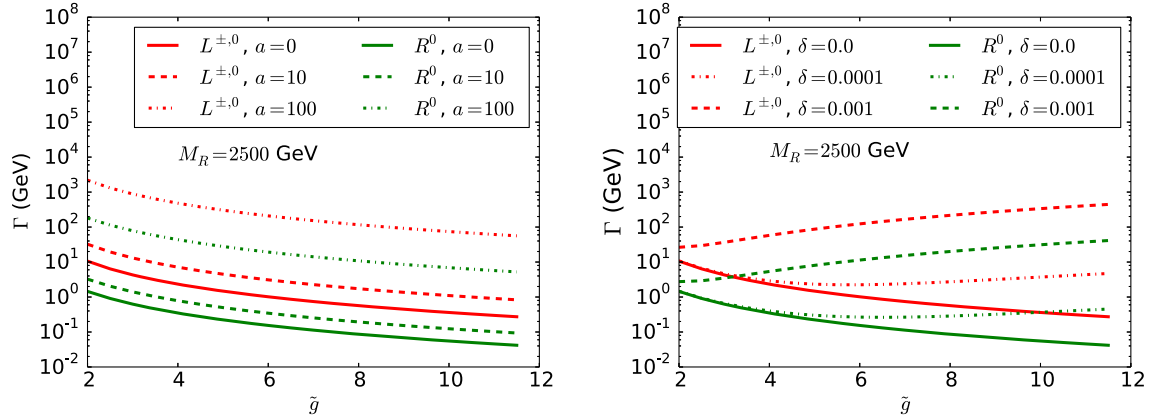
FIG. 6 (color online).   Widths of the heavy CVM vector resonances as a function of $\tilde{g}$ for different values of a (left) and δ (right). We keep $M_R = 2.5$ TeV fixed.

the charged. These choices of K factors mean that our exclusion limits are slightly conservative.[2]

As explained in the previous section, the masses of the heavy resonances are degenerate for large $\tilde{g}$ and only become appreciably different when $\tilde{g} \lesssim 1$. In fact, the left triplet $L^{0,\pm}$ states remain highly degenerate for all parameter values. The vector spectrum as a function of $\tilde{g}$ can be seen in Fig. 5. The corresponding widths are shown in Fig. 6 as a function of $\tilde{g}$ for different values of δ (left panel) and a (right panel) for $M_R = 2.5$ TeV. For fixed a the widths simply scale as $\Gamma \sim \frac{1}{\tilde{g}^2}$ as noted in Eq. (16).

For small values of a the partial widths $\Gamma_{\mathcal{R}_i}^{HW/HZ}$ are small compared to the other decay channels. In this case, the heavy resonances are very narrow and the separation in masses between the two neutral resonances is always larger than their widths. Furthermore the branching ratios are nearly constant as a function of $\tilde{g}$ and M_R, apart from corrections due to the mass differences of the final states.

Once a grows, the $HW^\pm/HZ$ channels become important and eventually dominate the widths of the heavy resonances. This phenomenon is shown at the branching ratios level as a function of a in Fig. 7. For fixed a the branching ratios are constant to leading order in M_R and $\tilde{g}$.

A. Dilepton searches

The current ATLAS [20] and CMS [19] exclusion limits on neutral vector resonances in the dilepton channels are based on modeling the signal as a single resonance. In the CVM, the two resonances are nearly degenerate as shown in Fig. 5. Two questions then arise: Is it possible to resolve a two-peak structure? And, is it possible to resolve the line shape of each peak?

The fractional dimuon mass resolution at CMS is $\sigma(\mu\mu)/m_{\mu\mu} \simeq 6.5\%$ at masses around 1 TeV. It further depletes at higher energies due to the difficulty in measuring the curvature of the track in the muon chambers. The dieletron mass resolution, $\Delta(m_{ee})/m_{ee}$,[3] on the other hand, is approximately constant above 500 GeV [49].[4] Summarizing, for heavy resonances whose widths are lower than 5% of their masses, the search is currently dominated by the resolution of the detector and therefore the line shapes of the peaks cannot be measured [20].

For values of $a \lesssim 1$ (or $\delta \lesssim 10^{-3}$) the ratio of the total width of the vector resonances to their mass satisfies $\Gamma_\mathcal{R}/m_\mathcal{R} \simeq 0.01$–0.1% which is well below the current sensitivity. This is illustrated in Fig. 8, showing the resonance pattern of the CVM in dilepton invariant mass distributions with two different bin widths—the largest bin width of 30 GeV is representative of current experimental sensitivity and insufficient to reconstruct the line shapes. We next consider the ability to resolve the two-peak structure. The relative mass splitting of our resonances is approximately

$$\frac{\Delta M}{M_R} \simeq \frac{0.16}{\tilde{g}^2}, \qquad \Delta M = |M_{L^0} - M_{R^0}|. \qquad (33)$$

This shows that the resolution of the detector would allow probing the presence of two peaks if $\tilde{g} \lesssim 2$.[5] This would also allow a measurement of $\tilde{g}$ directly from the separation of the two peaks.

---

[2]These choices correspond to the smallest K factors used by ATLAS and CMS in the resonance mass range from 1 to 3 TeV— the variation of K factors in this mass range for the neutral resonances are $K = 1.16$–1.22 [20] and for the charged resonances $K = 1.2$–1.3 [48].

[3]The different symbols σ and Δ indicate that the muon uncertainty follows a Gaussian while the electron uncertainty does not.

[4]When both electrons are detected in the barrel, this mass resolution is 1.1%, and when one of the electrons is in the barrel and the other is in the endcaps it is 2.3% [49].

[5]It may eventually be possible to probe them in the electron channel up to $\tilde{g} = 4$.
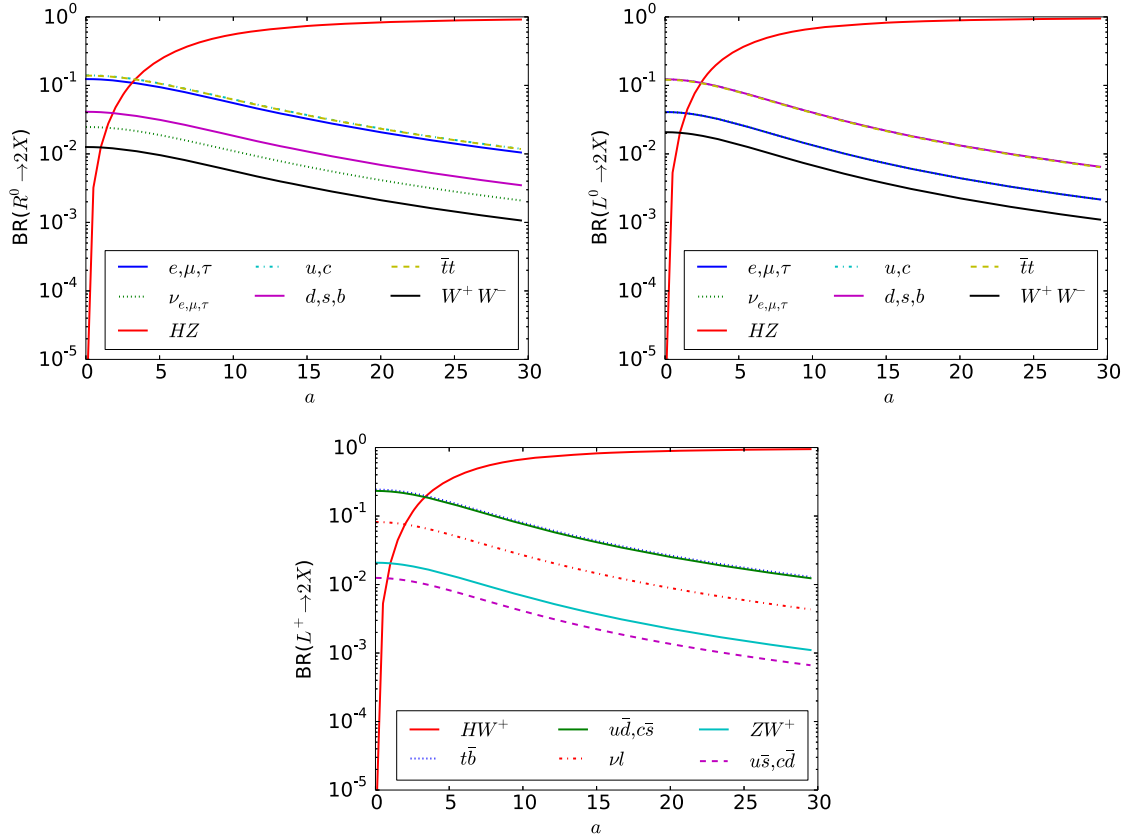
FIG. 7 (color online).   Branching ratios of the heavy CVM vector resonances R^0, L^0, and L^+.

For values of $a \gtrsim 1$ (or $\delta \gtrsim 10^{-3}$) the resonances can overlap. Values of $\Delta M/\bar{\Gamma}$, where $\bar{\Gamma} = (\Gamma_{L^0} + \Gamma_{R^0})/2$, as well as the largest Γ/M ratio are shown in Fig. 9. When $\Delta M/\bar{\Gamma}$ approaches unity, the resonances will overlap in the dilepton invariant mass distributions. This is shown in the right panel of Fig. 10. Furthermore the width over mass ratio exceeds unity for large a at which point the effective description breaks down.

Finally the interference between the signal and the SM background can be relevant. As seen in Fig. 8 the CVM features a destructive interference between the resonances and the SM background yielding a dip just before the peaks. If the dip and the resonance peak are summed into one bin obviously this can reduce the observed cross section at the peak. The effect of interference in dilepton resonant searches has been extensively studied in [50].
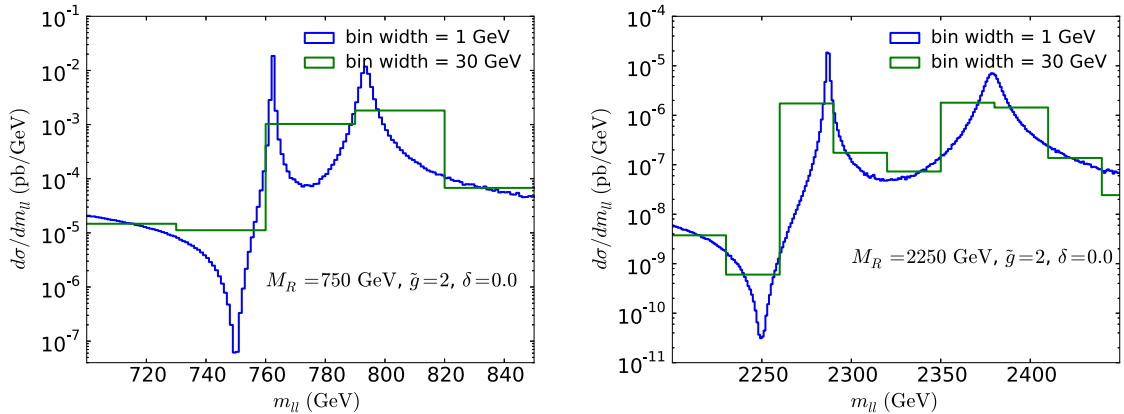

FIG. 8 (color online).   Dilepton invariant mass distributions, $M(\ell\ell)$, in the CVM, with 1 GeV (blue) and 30 GeV (green) binning. On the (left) $M_R = 750$ GeV and on the (right) $M_R = 2250$ GeV.
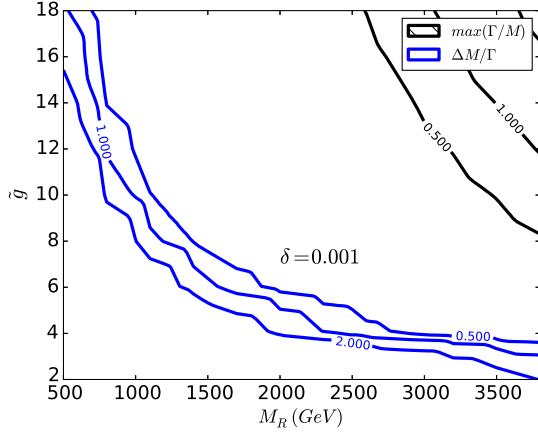
FIG. 9 (color online). Lines of constant mass splitting relative to width $\frac{\Delta M}{\Gamma}$ (blue lines) of the CVM resonances relative to their width as well as lines of constant maximal resonance width relative to mass max$[\Gamma/M]$ (black lines), in the plane $(M_R, \tilde{g})$.
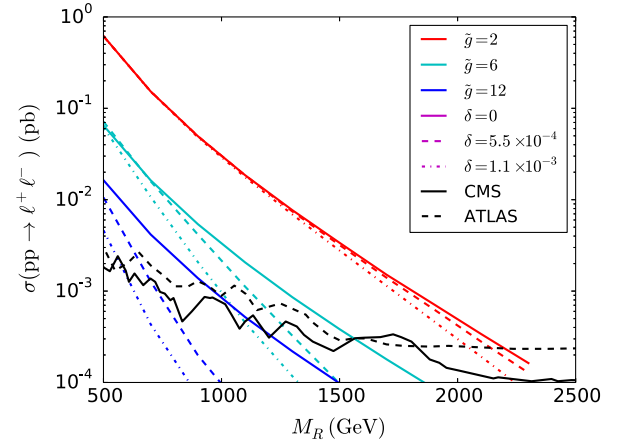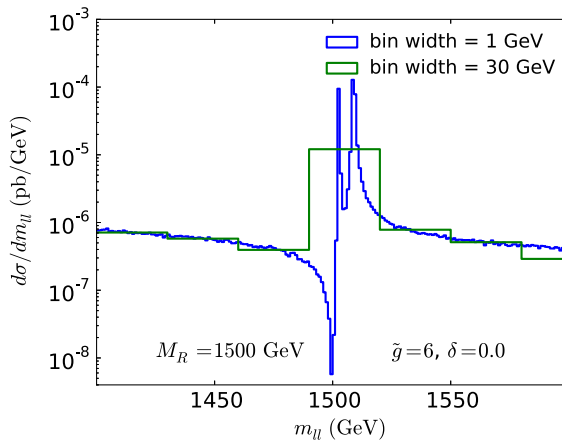

FIG. 11 (color online). Full LHC signal cross section for dilepton $\ell^+\ell^-$ production in the CVM with $\sqrt{s} = 8$ TeV at parton level as a function of M_R for different values of $\tilde{g}$ and δ as given in the figure. Also shown in black are the 95% exclusion limits provided by ATLAS and CMS [19,20].

Given the caveats above, a sound strategy to set relevant constraints is to consider first the case $\tilde{g} \gtrsim 2$ and *a* not too large. Here the peaks cannot be resolved and an overall cross section constraint can be set. Specifically, we compare the predicted cross section corresponding to the total number of events in the mass range $M(\ell\ell) > M_R$–30 GeV to the experimentally observed cross section limit.

In Fig. 11 we present the CVM dilepton cross section as a function of M_R for different values of $\tilde{g}$ and *a* together with the ATLAS and CMS 95% exclusion limits with center-of-mass energy $\sqrt{s} = 8$ TeV and $L \approx 20$ fb^{-1} of integrated luminosity [19,20].

1. Off-diagonal widths

In the parameter range where the resonances overlap, their off-diagonal widths can also become important—i.e., the imaginary and real parts of the vector resonance self-energies cannot be diagonalized simultaneously—and

contribute to the amplitude. The basic formalism was recently discussed in [51], and we review it in Appendix D.

The contributions of fermion and vector loops to the imaginary parts of the vector self-energies are reported in [51], while the Higgs contribution from the diagrams in Fig. 12 are given by

$$\Sigma_H^{\mathcal{R}}(p^2) = (g_{\mathcal{R}_i ZH})(g_{\mathcal{R}_j ZH}) \frac{\sqrt{\lambda(p^2, M_H^2, M_Z^2)}}{16\pi p^2}$$
$$\times \left[1 + \frac{1}{12 M_Z^2 p^2} \lambda(p^2, M_H^2, M_Z^2)\right], \qquad (34)$$

where $\lambda(x, y, z) = x^2 + y^2 + z^2 - 2xy - 2yz - 2zx$. Notice that these diagrams contribute only to the transverse part of the self-energy, Π_T of Eq. (D1). In the CVM the Higgs contribution dominates the of-diagonal widths.
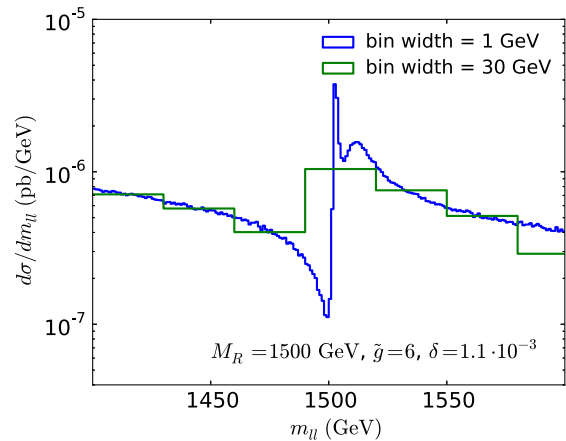

FIG. 10 (color online). Dilepton invariant mass distributions, $M(\ell\ell)$, in the CVM, for fixed $M_R = 1500$ GeV with 1 GeV (blue) and 30 GeV (green) binning. On the (left) $\delta = 0$ and on the (right) $\delta = 10^{-3}$.
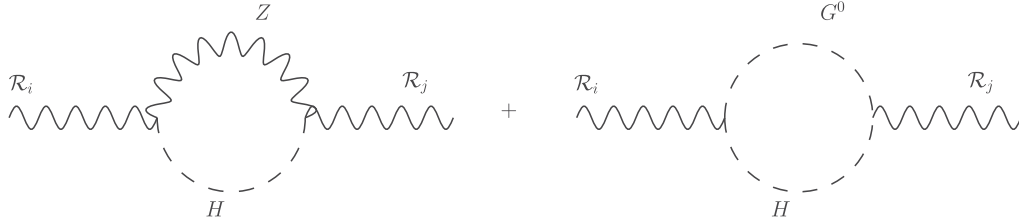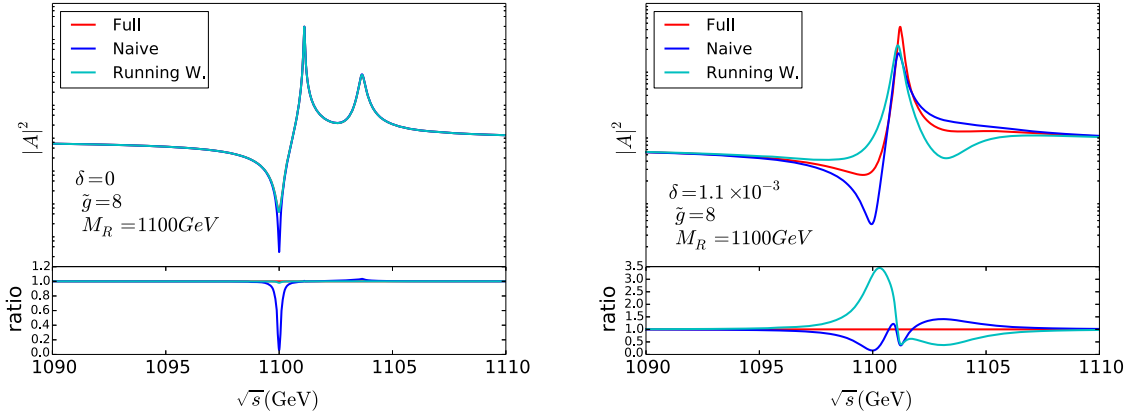
FIG. 12. One-loop heavy vector self-energy diagrams in the CVM with internal Higgs bosons contributing to the off-diagonal widths.

FIG. 13 (color online). The amplitude squared, summed and averaged over color and spin of the process $u\bar{u} \to e^+ e^-$ with the contribution of the two heavy particles and interference (background from Z and photon contribution is subtracted) for three different computational schemes (see text for more details). On the left (right) panel $\delta = 0$ ($\delta = 10^{-3}$). The ratio between each scheme to the *full* amplitude is shown on the bottom inserts.
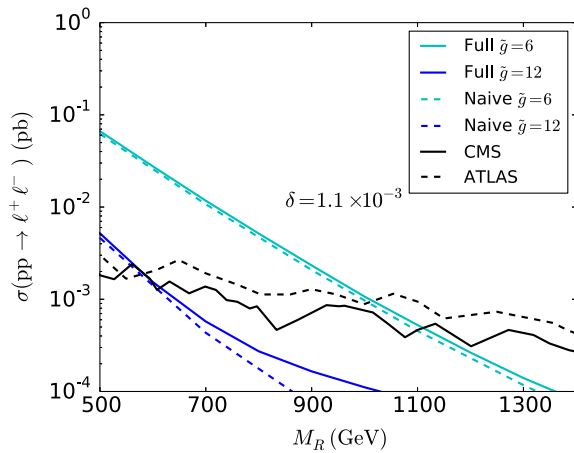
In Fig. 13 we illustrate the effect of the of-diagonal widths. We show the amplitude squared, summed and averaged over color and spin for the process $u\bar{u} \to L^0/R^0 \to e^+ e^-$ (i.e., excluding purely SM contributions

FIG. 14 (color online). Full LHC signal cross section for dilepton $\ell^+ \ell^-$ production in the CVM with $\sqrt{s} = 8$ TeV at parton level, taking into account off-diagonal widths, as a function of M_R for different values of $\tilde{g}$ and δ as given in the figure. Also shown in black are the 95% exclusion limits provided by ATLAS and CMS [19,20].

from Z and γ) in three different schemes: In the *naive* computation the propagators are added with a fixed width; in the *running W* computation each propagator is included with the energy dependent width; and in the *full* computation, the complete amplitude including off-diagonal widths is used. The ratio between each scheme to the *full* amplitude is shown on the bottom inserts. When δ is large, the difference between the *naive* and the *full* computation can be of the order of 50% close to the resonance peaks.

Nevertheless, the corresponding exclusion limits derived with the full scheme are only a bit stronger as can be seen by comparing Figs. 11 and 14.

B. Single charged lepton searches

In the CVM, only the $L^{\pm}$ resonances contribute to the single charged lepton final states $\ell\nu$. However, properly accounting for interference effects with the SM states in these channels is delicate; see e.g., [52]. Due to the final state neutrino, one has to rely on the smeared transverse mass distribution to infer the presence of the new resonance, as opposed to the narrower peaks in the dilepton invariant mass distribution. The interference in the low energy part of the transverse mass distribution can be significant. For this reason the CMS Collaboration also
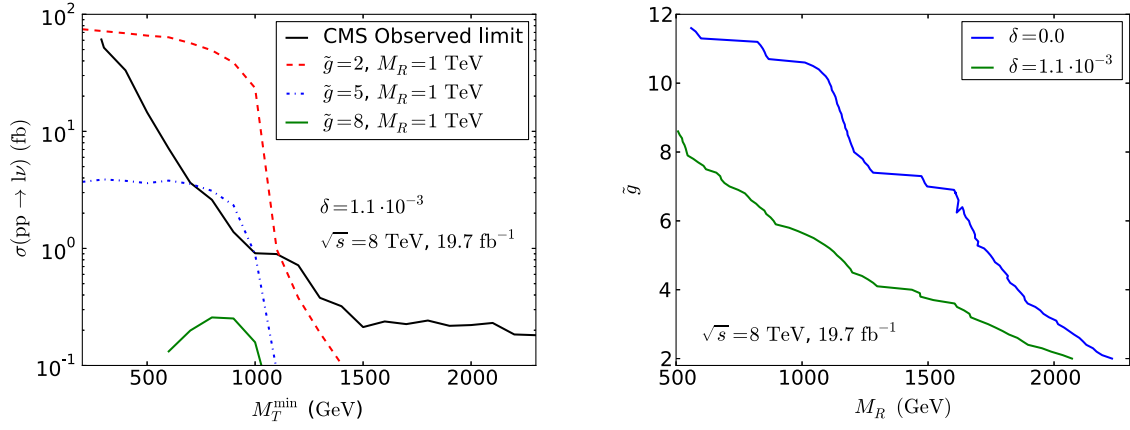
FIG. 15 (color online). Left: full LHC signal cross section for single charged lepton $\ell\nu_\ell$ production in the CVM with $\sqrt{s} = 8$ TeV at parton level for fixed $M_R = 1$ TeV as a function of the transverse mass cut $M_T^{\min}$. Also shown is the 95% confidence level exclusion limit observed by CMS [48]. Right: the corresponding exclusion limit on the CVM in the $(M_R, \tilde{g})$ plane for two different values of δ.
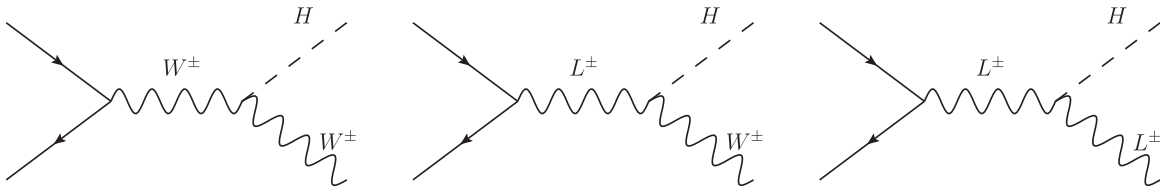

FIG. 16. Feynman diagrams contributing to Higgs production in association with charged vectors in the CVM.
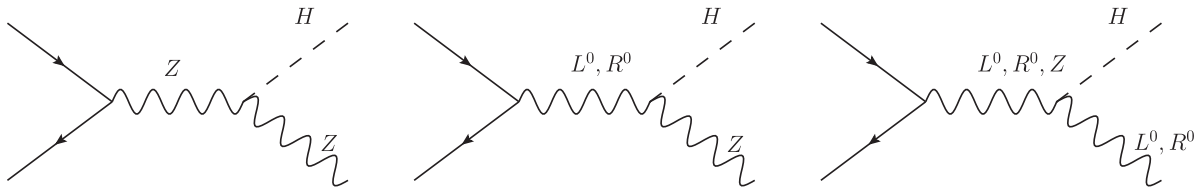
FIG. 17. Feynman diagrams contributing to Higgs production in association with neutral vectors in the CVM.
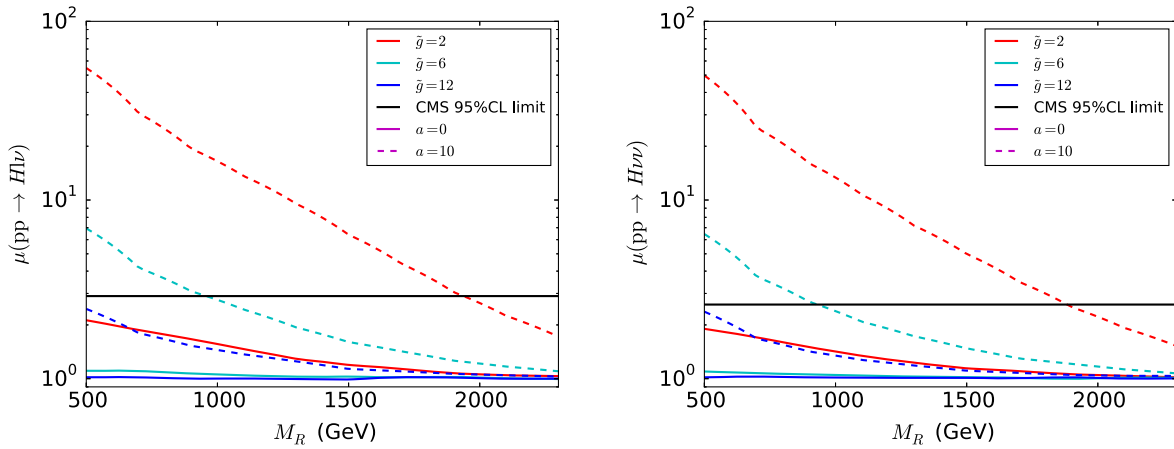
FIG. 18 (color online). The value of the signal strength $\mu = \sigma_{\mathrm{CVM}}/\sigma_{\mathrm{SM}}$ at the LHC with $\sqrt{s} = 8$ TeV for the processes $pp \to H\ell\nu$ (left) and $pp \to H\nu\nu$ (right) as a function of M_R for different values of the CVM parameters $\tilde{g}, a$. Also shown are exclusion limits from CMS on μ in the $W(\ell\nu, \tau\nu)H(b\bar{b})$ channels (black).

FIG. 19 (color online).   95% exclusion limits on the CVM from LHC shown in $(M_R, \tilde{g})$ planes for fixed δ (upper) and fixed a (lower) values. Shown are the limits from dilepton searches (blue), limits from single char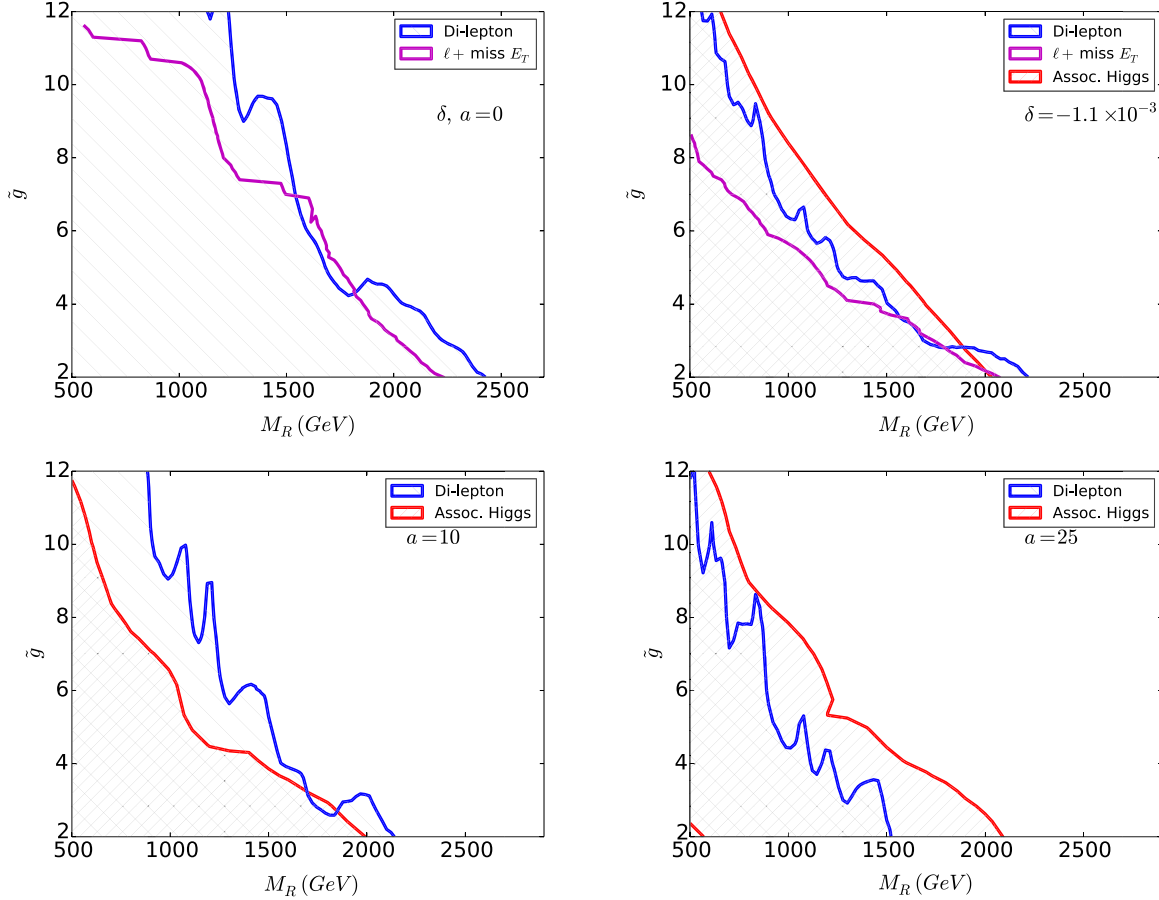ged lepton searches (purple), and limits for associated Higgs production (red). The striped and cross striped regions are excluded.

provides exclusion limits as a function of the minimum transverse mass cut $M_T^{\min}$ [48].[6]

The corresponding ATLAS analysis [53] does not show exclusion limits as a function of the transverse mass cut. Therefore we only use the CMS limits. The CMS exclusion limit we present is obtained with the 2012 data set of $L = 19.7$ fb^{-1} at $\sqrt{s} = 8$ TeV. On the left-hand side of Fig. 15 the 95% confidence level exclusion limit as a function of the minimum transverse mass cut is presented together with model predictions for different values of $\tilde{g}$ and δ with $M_R = 1$ TeV. On the right-hand side the exclusion is translated into the $(M_R, \tilde{g})$ plane for fixed values of δ— for each value of M_R we choose the value of $M_T^{\min}$ that yields the strongest limit.

C. Associated Higgs searches

Current searches for the production of the Higgs state in association with a SM vector boson also yield relevant bounds on the CVM parameter space. The ATLAS and CMS collaborations provide upper bounds on the signal strength $\mu = \sigma/\sigma_{\mathrm{SM}}$, for the processes $pp \to H(b\bar{b})Z(\ell^+\ell^-)$, $pp \to H(b\bar{b})Z(\nu\nu)$, and $pp \to H(b\bar{b})W(\ell\nu, \tau\nu)$ [25,26].

In the CVM the final state vector resonance can be any of the states $V = Z, W^\pm$ or $\mathcal{R}_i = L^{0,\pm}, R^0$ and the relevant diagrams are shown in Figs. 16 and 17. The largest contribution to the CMS analysis of the $pp \to H(b\bar{b})W(\ell\nu, \tau\nu)$ channel typically comes from $HL^\pm$ production even though it is phase space suppressed with respect to $HW^\pm$. This is due to the large $HL^\pm L^\mp$ coupling [Eq. (B14)]. Moreover, the kinematical cuts employed in the analysis tend to enhance the high energy region and consequently the new physics contribution. The CMS best-fit signal strength with 1-sigma errors is

$$\mu(W(\ell\nu, \tau\nu)H) = 1.1 \pm 0.9. \qquad (35)$$

In the corresponding ATLAS analysis of $pp \to H(b\bar{b})W(\ell\nu, \tau\nu)$ the transverse mass system associated with the W boson (lepton and missing energy) is required to be small,

---

[6]Notice that the problem is not only how to define the signal region; the importance of the low energy interference will also affect the control regions since they need to be signal free.
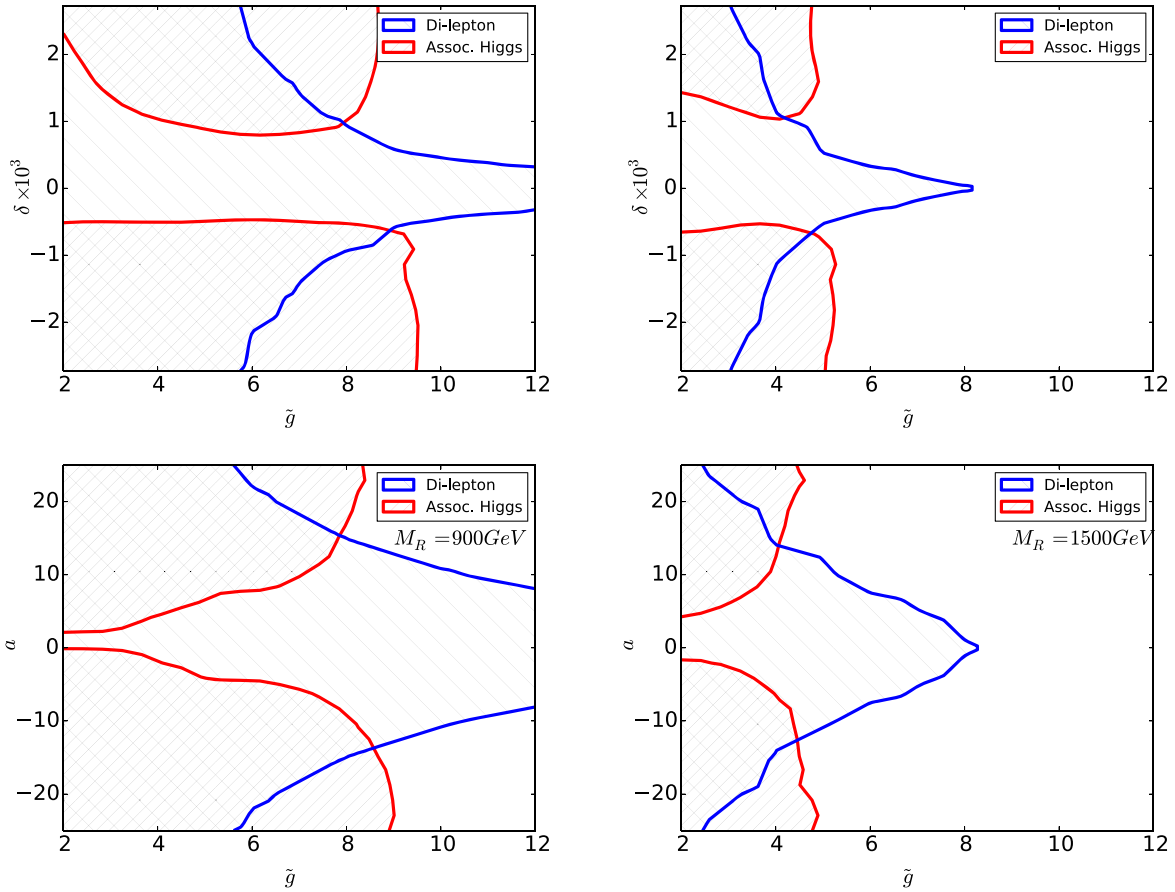
FIG. 20 (color online). 95% exclusion limits as above, but in $(\delta, \tilde{g})$ (left) and $(a, \tilde{g})$ (right) planes for fixed M_R values.

$m_T^W < 120$ GeV, which strongly reduces contributions from the CVM vector resonances. Therefore, we use the CMS result to set limits on the CVM parameter space.

For the $pp \to H(b\bar{b})Z(\nu\nu)$ search the HL^0 channel gives the largest contribution of new physics in both the CMS and ATLAS analysis. Again we choose to use the CMS result

$$\mu(Z(\nu\nu)H) = 1.0 \pm 0.8, \qquad (36)$$

to impose limits on the CVM.[7]

In the search for $pp \to H(b\bar{b})Z(\ell^+\ell^-)$ the mass of the dilepton system is required to be near M_Z and therefore the HL^0/HR^0 channels are highly off-shell and suppressed. It is thus neglected here. It would be very interesting to consider a dedicated analysis looking for resonances in the dilepton mass system in this search channel as proposed in [9,10,54–56].

_____
[7]The ATLAS result in this search channel gives the unphysical result $\mu(Z(\nu\nu)H) = -0.3 \pm 0.5$ which essentially excludes both the SM and CVM at the 95% confidence level. However, since a 2-sigma level deficit is also observed in the control sample $\mu(Z(\ell\ell)Z(b\bar{b}))$ and no deficit is observed in the search channel $\mu(Z(\ell\ell)H)$, we disregard the result.

To set our limits we use the total CVM cross section in the associated Higgs channels. We again believe this yields a conservative limit since the cuts employed in [25] select high energy events and enhance the new CVM contribution with respect to the SM.

On the left-hand side of Fig. 18 we show the predicted signal strength, $\mu = \sigma/\sigma_{\rm SM}$ in the $pp \to H\ell\nu$ channel for different CVM parameters. The exclusion limit on μ shown in the figure comes from the measurement of $H(b\bar{b})W(\tau\nu, \ell\nu)$ at CMS. Analogously, the signal strength of the $pp \to H\nu\bar{\nu}$ process in CVM is shown on the right-hand side of Fig. 18 with the corresponding exclusion limits derived from the $H(b\bar{b})Z(\nu\bar{\nu})$ channel.

As expected the limits are stronger than the ones from dilepton searches for large values of a. Moreover, a dedicated resonance search in these channels could provide more stringent limits on the parameter space. Or better, the chance to discover the interplay of multiple resonances with the Higgs boson.

D. Parameter space

We end this section by studying the allowed regions in the $M_R, \tilde{g}$ and a parameter space given the constraints from dilepton $\ell^+\ell^-$ (blue curves), single-charged lepton
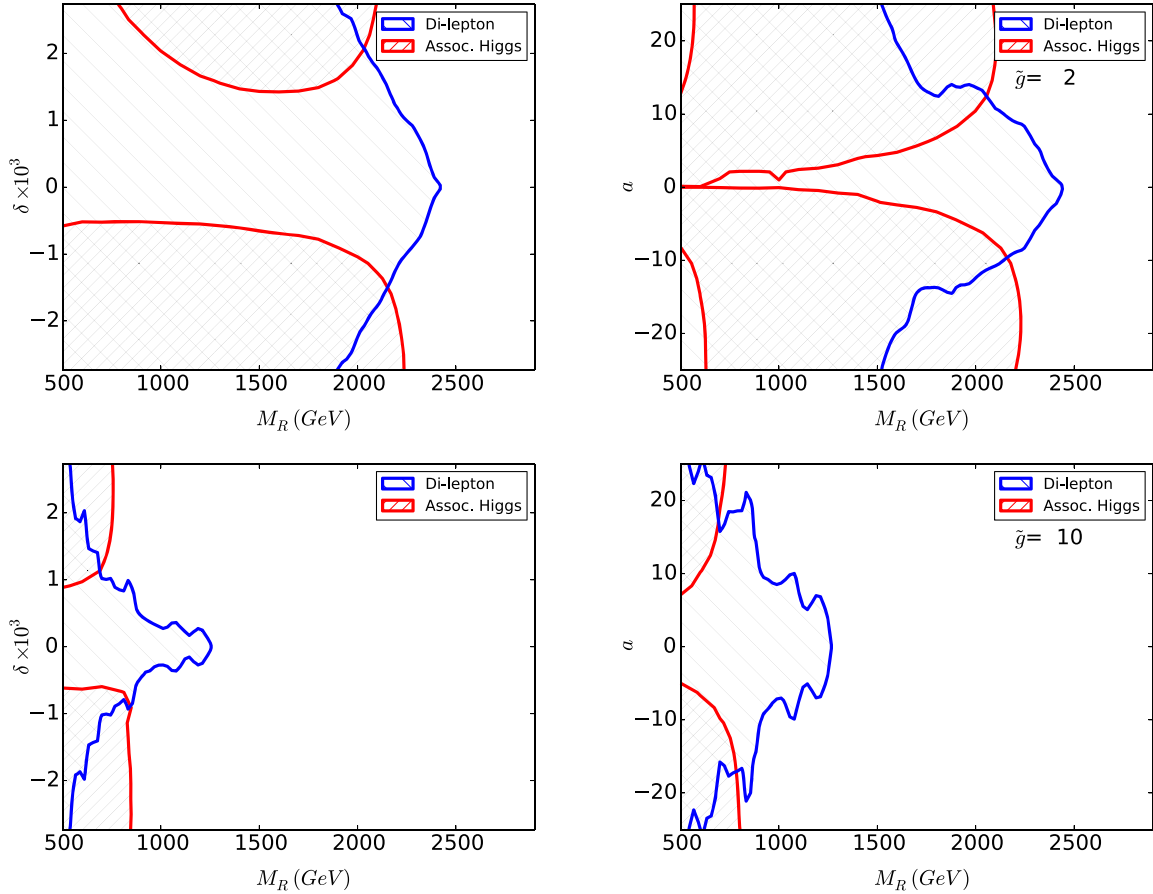
FIG. 21 (color online). 95% exclusion limits as above but in (δ, M_R) (left) and (a, M_R) (right) planes for fixed $\tilde{g}$ values.
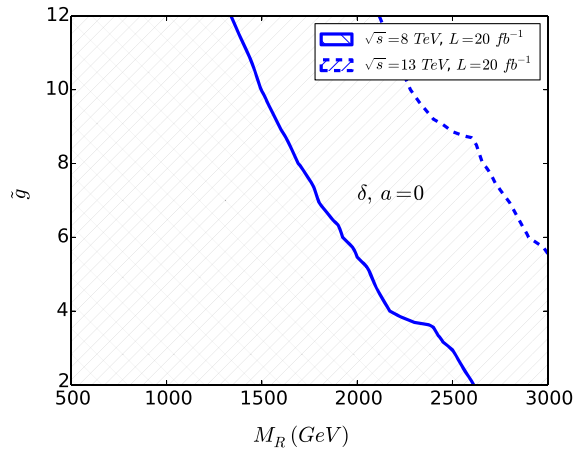

FIG. 22 (color online). Projected discovery reach or exclusion limit of the LHC Run II dilepton resonance search at $\sqrt{s} = 13$ TeV with $L = 20$ fb^{-1} in the $(M_R, \tilde{g})$ plane (dashed blue). The striped and cross striped regions will be excluded in the absence of discovery. Also shown is the equivalently projected exclusion limit for the current run at $\sqrt{s} = 8$ TeV (solid blue) to assess the validity of the projection.

$\ell^{\pm} + \cancel{E}_T$ (magenta curves), and associated Higgs searches[8] (red curves). In some of the plots we show the parameter δ instead of a.

The allowed and excluded regions at 95% C.L. are shown as the white and striped regions, respectively, in $(M_R, \tilde{g})$ planes in Fig. 19 for fixed values of a or δ. For $a = 0$ only the dilepton and (subdominantly) the single charged lepton searches significantly constrain the parameter space as shown in the upper left panel of Fig. 19. However, a dedicated study may put further constraints via the nonzero $HL^{\pm}L^{\pm}$ interaction giving rise to diagram 3 in Fig. 16. As a is dialed up, associated Higgs production starts to compete with the dilepton searches as shown in the three remaining panels. In particular for $a \gtrsim 20$ ($|\delta| \gtrsim 10^{-3}$) the associated Higgs production provide the strongest constraint over most of the parameter space shown.

The same can be seen from the exclusion limits in the $(\delta, \tilde{g})$ and $(a, \tilde{g})$ planes for different values of M_R shown in Fig. 20. Finally, in Fig. 21 we show the regions in (M_R, a) and (M_R, δ) planes for different values of $\tilde{g}$.

---

[8]We use a simple χ^2 analysis to combine the $H\ell\nu$ and $H\nu\nu$ channels.

In summary, the LHC currently excludes roughly between a third or half of the parameter space satisfying $\tilde{g} < 4\pi$ and $M_R \lesssim \tilde{g}v \simeq 3$ TeV and $|a| \lesssim 25$. The constraints from electroweak precision measurements are negligible in comparison, due to the enhanced global $SU(2)'_L \times SU(2)'_R$ symmetry over the vector spectrum.

1. Future reach

We show an estimate of the CMS reach in the dilepton channel at the high energy Run II of LHC at $\sqrt{s} = 13$ TeV in Fig. 22. For comparison with the upper left panel of Fig. 19 we also show the estimated current LHC exclusion curve using the method detailed in Appendix E. Although the computation is simplistic, it compares reasonably well and we therefore expect the projection to be a good guide to the future run. For $a = 0$ most of the parameter space will be excluded already with $L = 20$ fb^{-1} while $L = 100$ fb^{-1} will be enough to exclude the entire parameter space shown. To exclude the same values of $(M_R, \tilde{g})$ for $|a| \lesssim 10$ the required luminosity is estimated to be $L = 200$ fb^{-1}.

VI. SUMMARY AND OUTLOOK

In this paper we have presented the custodial vector model, featuring two new weak triplets of vector resonances in addition to the SM and three new parameters determining their interactions. Here we have studied the CVM in its own right but as mentioned in the Introduction the model can be interpreted as an effective Lagrangian for several different theories of dynamical EWSB.

We have further discussed the distinct collider phenomenology of the CVM: the presence of two nearly mass degenerate resonances in dilepton final states and a single (dominant) resonance in single charged lepton final states as well as the apparent absence of resonances in the WW and WZ channels. Finally the interactions between the new resonances and the Higgs sector can be probed by the associate Higgs production.

Despite the simple and distinct pattern of resonances, the identification of the CVM at LHC is challenging because of suppressed couplings to SM fields for $\tilde{g} > 1$, the narrow spacing of the resonances and, in a significant part of the

parameter space, their narrow widths. Given the CVM, Run II of the LHC should be able to discover a signal of new physics from the vector resonances with about 200 inverse femtobarns of luminosity in the parameter space region $M_R < 3$ TeV, $\tilde{g} < 4\pi$, and at least $|a| \lesssim 10$. However, to clearly identify the new physics as stemming from the CVM, more luminosity and better resolution will be required. A high energy lepton collider would be ideal to uncover the CVM.

ACKNOWLEDGMENTS

APPENDIX A: MASS MATRICES

The spin-one mass Lagrangian is

$$\mathcal{L}_{\text{mass}} = (\tilde{W}^-_\mu \quad A^-_{L\mu} \quad A^-_{R\mu})\mathcal{M}^2_C \begin{pmatrix} \tilde{W}^{+\mu} \\ A^{+\mu}_L \\ A^{+\mu}_R \end{pmatrix}$$

$$+ \frac{1}{2}(B_\mu \quad \tilde{W}^3_\mu \quad A^0_{L\mu} \quad A^0_{R\mu})\mathcal{M}^2_N \begin{pmatrix} B^\mu \\ \tilde{W}^{3\mu} \\ A^{0\mu}_L \\ A^{0\mu}_R \end{pmatrix}, \quad \text{(A1)}$$

where

$$\mathcal{M}^2_C = \begin{pmatrix} g^2 \frac{f^2+(1+s)v^2}{4} & -g\tilde{g}\frac{f^2+sv^2}{4} & 0 \\ -g\tilde{g}\frac{f^2+sv^2}{4} & \tilde{g}^2\frac{f^2+sv^2}{4} & 0 \\ 0 & 0 & \tilde{g}^2\frac{f^2+sv^2}{4} \end{pmatrix},$$

(A2)

$$\mathcal{M}^2_N = \begin{pmatrix} g'^2 \frac{f^2+(1+s)v^2}{4} & -gg'\frac{v^2}{4} & 0 & -g'\tilde{g}\frac{f^2+sv^2}{4} \\ -gg'\frac{v^2}{4} & g^2\frac{f^2+(1+s)v^2}{4} & -g\tilde{g}\frac{f^2+sv^2}{4} & 0 \\ 0 & -g\tilde{g}\frac{f^2+sv^2}{4} & \tilde{g}^2\frac{f^2+sv^2}{4} & 0 \\ -g'\tilde{g}\frac{f^2+sv^2}{4} & 0 & 0 & \tilde{g}^2\frac{f^2+sv^2}{4} \end{pmatrix}.$$

(A3)

The charged mass eigenstates are the W boson, $L^\pm$, and $R^\pm$, whereas the neutral mass eigenstates are the photon A, the Z boson, L^0 and R^0. Let $\mathcal{C}$ and $\mathcal{N}$ be the charged and neutral rotation matrix, respectively:

$$\begin{pmatrix} \tilde{W}^\pm_\mu \\ A^\pm_{L\mu} \\ A^\pm_{R\mu} \end{pmatrix} = \mathcal{C} \begin{pmatrix} W^\pm_\mu \\ L^\pm_\mu \\ R^\pm_\mu \end{pmatrix}, \qquad \begin{pmatrix} \tilde{B}_\mu \\ \tilde{W}^3_\mu \\ A^3_{L\mu} \\ A^3_{R\mu} \end{pmatrix} = \mathcal{N} \begin{pmatrix} A_\mu \\ Z_\mu \\ L^0_\mu \\ R^0_\mu \end{pmatrix}. \qquad (A4)$$

Diagonalization of the charged-boson mass matrix gives

$$M^2_W = \frac{g^2 + \tilde{g}^2}{\tilde{g}^2} \frac{M^2_R}{2} + \frac{g^2 v^2}{8}$$
$$- \sqrt{\left(\frac{g^2 + \tilde{g}^2}{\tilde{g}^2} \frac{M^2_R}{2} + \frac{g^2 v^2}{8} \right)^2 - \frac{g^2 v^2 M^2_R}{4}},$$

$$M^2_{R^\pm} = M^2_R,$$

$$M^2_{L^\pm} = \frac{g^2 + \tilde{g}^2}{\tilde{g}^2} \frac{M^2_R}{2} + \frac{g^2 v^2}{8}$$
$$+ \sqrt{\left(\frac{g^2 + \tilde{g}^2}{\tilde{g}^2} \frac{M^2_R}{2} + \frac{g^2 v^2}{8} \right)^2 - \frac{g^2 v^2 M^2_R}{4}}, \qquad (A5)$$

where M_R is defined in Eq. (17),

$$\mathcal{C} = \begin{pmatrix} \cos\alpha & -\sin\alpha & 0 \\ \sin\alpha & \cos\alpha & 0 \\ 0 & 0 & 1 \end{pmatrix},$$

$$\sin\alpha = \sqrt{\frac{M^2_{L^\pm} - M^2_{R^\pm}}{M^2_{L^\pm} - M^2_W}} = \frac{g}{\tilde{g}} + \mathcal{O}\left(\frac{g^3}{\tilde{g}^3} \right). \qquad (A6)$$

Note that the spin-one charged resonance associated with the $SU(2)_R$ group does not mix with the W boson, and its mass is therefore unaffected, at tree level, by the electroweak interactions. The $SU(2)_L$ resonance does mix with the W boson, and its mass receives a small and positive contribution.

The 4×4 neutral mass matrix can be diagonalized analytically, because one eigenvalue is the massless photon. However, it is more instructive to expand eigenvalues and eigenvectors in powers of $1/\tilde{g}$, assuming that M_R scales as $\tilde{g}$ without a parametric suppression from $f^2 + sv^2$. This gives

$$M^2_Z = \frac{g^2 + g'^2}{4} v^2 \left[1 - \frac{g^4 + g'^4}{(g^2 + g'^2)\tilde{g}^2} + \mathcal{O}\left(\frac{g^4}{\tilde{g}^4} \right) \right],$$

$$M^2_{R^0} = M^2_R \left[1 + \frac{g'^2}{\tilde{g}^2} + \mathcal{O}\left(\frac{g^4}{\tilde{g}^4} \right) \right],$$

$$M^2_{L^0} = M^2_R \left[1 + \frac{g^2}{\tilde{g}^2} + \mathcal{O}\left(\frac{g^4}{\tilde{g}^4} \right) \right]. \qquad (A7)$$

Note that the $SU(2)_L$ neutral resonance is still heavier than its $SU(2)_R$ counterpart, as $g > g'$. The elements of the neutral boson rotation matrix are

$$\mathcal{N}_{00} = \frac{e}{g'}, \qquad \mathcal{N}_{10} = \frac{e}{g}, \qquad \mathcal{N}_{20} = \frac{e}{\tilde{g}}, \qquad \mathcal{N}_{30} = \frac{e}{\tilde{g}},$$

$$\mathcal{N}_{01} = -\frac{g'}{\sqrt{g^2 + g'^2}} \left[1 + \frac{g^4 - 2g^2 g'^2 - g'^4}{2(g^2 + g'^2)\tilde{g}^2} + \mathcal{O}\left(\frac{g^4}{\tilde{g}^4} \right) \right],$$

$$\mathcal{N}_{11} = \frac{g}{\sqrt{g^2 + g'^2}} \left[1 + \frac{g'^4 - 2g^2 g'^2 - g^4}{2(g^2 + g'^2)\tilde{g}^2} + \mathcal{O}\left(\frac{g^4}{\tilde{g}^4} \right) \right],$$

$$\mathcal{N}_{21} = \frac{g^2}{\sqrt{g^2 + g'^2}\tilde{g}} \left[1 + \mathcal{O}\left(\frac{g^2}{\tilde{g}^2} \right) \right], \qquad \mathcal{N}_{31} = -\frac{g'^2}{\sqrt{g^2 + g'^2}\tilde{g}} \left[1 + \mathcal{O}\left(\frac{g^2}{\tilde{g}^2} \right) \right],$$

$$\mathcal{N}_{02} = \frac{v^2 g' g^4}{4\tilde{g} M^2_R (g^2 - g'^2)} \left[1 + \mathcal{O}\left(\frac{g^2}{\tilde{g}^2} \right) \right], \qquad \mathcal{N}_{12} = -\frac{g}{\tilde{g}} \left[1 + \mathcal{O}\left(\frac{g^2}{\tilde{g}^2} \right) \right],$$

$$\mathcal{N}_{22} = 1 - \frac{g^2}{2\tilde{g}^2} + \mathcal{O}\left(\frac{g^4}{\tilde{g}^4} \right), \qquad \mathcal{N}_{32} = -\frac{g^2 g'^2 v^2}{4(g^2 - g'^2) M^2_R} \left[1 + \mathcal{O}\left(\frac{g^2}{\tilde{g}^2} \right) \right],$$

$$\mathcal{N}_{03} = -\frac{g'}{\tilde{g}} \left[1 + \mathcal{O}\left(\frac{g^2}{\tilde{g}^2} \right) \right], \qquad \mathcal{N}_{13} = -\frac{v^2 g'^4 g}{4\tilde{g} M^2_R (g^2 - g'^2)} \left[1 + \mathcal{O}\left(\frac{g^2}{\tilde{g}^2} \right) \right],$$

$$\mathcal{N}_{23} = \frac{g^2 g'^2 v^2}{4(g^2 - g'^2) M^2_R} \left[1 + \mathcal{O}\left(\frac{g^2}{\tilde{g}^2} \right) \right], \qquad \mathcal{N}_{33} = 1 - \frac{g'^2}{2\tilde{g}^2} + \mathcal{O}\left(\frac{g^4}{\tilde{g}^4} \right). \qquad (A8)$$

APPENDIX B: COUPLINGS

In order to express the vertices with vectors in a compact form, we define

$$
\begin{pmatrix} \mathcal{W}_{1\mu}^{\pm} \\ \mathcal{W}_{2\mu}^{\pm} \\ \mathcal{W}_{3\mu}^{\pm} \end{pmatrix} \equiv \begin{pmatrix} W_{\mu}^{\pm} \\ L_{\mu}^{\pm} \\ R_{\mu}^{\pm} \end{pmatrix}, \qquad \begin{pmatrix} \mathcal{Z}_{0\mu} \\ \mathcal{Z}_{1\mu} \\ \mathcal{Z}_{2\mu} \\ \mathcal{Z}_{3\mu} \end{pmatrix} \equiv \begin{pmatrix} A_{\mu} \\ Z_{\mu} \\ L_{\mu}^{0} \\ R_{\mu}^{0} \end{pmatrix}. \tag{B1}
$$

The trilinear spin-one vertices are

$$
\mathcal{L}_{\mathcal{Z}WW} = \sum_{klm} g_{klm} ([[\mathcal{Z}_k \mathcal{W}_l^+ \mathcal{W}_m^-]] + [[\mathcal{W}_l^+ \mathcal{W}_m^- \mathcal{Z}_k]]) \tag{B2}
$$

where

$$
g_{klm} = g\mathcal{N}_{1k}\mathcal{C}_{1l}\mathcal{C}_{1m} + \tilde{g}(\mathcal{N}_{2k}\mathcal{C}_{2l}\mathcal{C}_{2m} + \mathcal{N}_{3k}\mathcal{C}_{3l}\mathcal{C}_{3m}). \tag{B3}
$$

The Higgs vertices with vectors are

$$
\mathcal{L}_{H\mathcal{V}\mathcal{V}} = \left(2\frac{H}{v} + \frac{H^2}{v^2} \right) \sum_{kl} \left[(\mathcal{C}^T \delta\mathcal{M}_C^2 \mathcal{C})_{kl} \mathcal{W}_{k\mu}^- \mathcal{W}_l^{+\mu} \right.
$$
$$
\left. + \frac{1}{2}(\mathcal{N}^T \delta\mathcal{M}_N^2 \mathcal{N})_{kl} \mathcal{Z}_{k\mu} \mathcal{Z}_l^{\mu} \right], \tag{B4}
$$

where $\delta\mathcal{M}_C^2$ and $\delta\mathcal{M}_N^2$ are the v^2 part of the charged and neutral mass matrices, respectively,

$$
\delta\mathcal{M}_C^2 = \begin{pmatrix} g^2 \frac{(1+s)v^2}{4} & -g\tilde{g}\frac{sv^2}{4} & 0 \\ -g\tilde{g}\frac{sv^2}{4} & \tilde{g}^2\frac{sv^2}{4} & 0 \\ 0 & 0 & \tilde{g}^2\frac{sv^2}{4} \end{pmatrix}, \tag{B5}
$$

$$
\delta\mathcal{M}_N^2 = \begin{pmatrix} g'^2\frac{(1+s)v^2}{4} & -gg'\frac{v^2}{4} & 0 & -g'\tilde{g}\frac{sv^2}{4} \\ -gg'\frac{v^2}{4} & g^2\frac{(1+s)v^2}{4} & -g\tilde{g}\frac{sv^2}{4} & 0 \\ 0 & -g\tilde{g}\frac{sv^2}{4} & \tilde{g}^2\frac{sv^2}{4} & 0 \\ -g'\tilde{g}\frac{sv^2}{4} & 0 & 0 & \tilde{g}^2\frac{sv^2}{4} \end{pmatrix}. \tag{B6}
$$

Finally, the SM fermions couple to the spin-one resonances through mixings with the electroweak bosons. This leads to the vertices

$$
\mathcal{L}_{\mathcal{V}ff} = \frac{g}{\sqrt{2}} \sum_k \sum_i \mathcal{C}_{1k}\bar{u}_i \mathcal{W}_k^+ P_L d_i + \text{H.c.}
$$
$$
+ \sum_k \sum_f (g\mathcal{N}_{1k} - g'\mathcal{N}_{0k})\bar{f}\mathcal{Z}_k
$$
$$
\times \left(T_f^3 P_L - \frac{g'^2}{g^2 + g'^2}Q_f \right)f
$$
$$
+ e\sum_f \bar{f}AQ_f f, \tag{B7}
$$

where i runs over quark and lepton doublets, with u_i (d_i) up-type (down-type) fermion, and f runs over all quark and lepton flavors.

Here we list the set of interactions between physical states relevant for the present study in the form presented in Sec. II. The expansions in $g/\tilde{g}$ assume that M_R scales as $\tilde{g}$ without parametric suppression from $f^2 + sv^2$, the a parameter is or order 1, and δ scales as $g^4/(\tilde{g}^2 M_R^2)$.

The couplings between L, R and SM weak bosons are

$$
g_{LWW}^{(1)} = g_{LWW}^{(2)} = g_{211} = \frac{g^4 v^2}{4\tilde{g}M_R^2} + \mathcal{O}\left(\frac{g^4}{\tilde{g}^4}\right),
$$

$$
g_{RWW}^{(1)} = g_{RWW}^{(2)} = g_{311} = \frac{g^2 g'^2 v^2}{4M_R^2\tilde{g}} + \mathcal{O}\left(\frac{g^4}{\tilde{g}^4}\right),
$$

$$
g_{ZLW}^{(1)} = g_{ZLW}^{(2)} = g_{121} = \frac{g^3\sqrt{g^2 + g'^2}v^2}{4\tilde{g}M_R^2} + \mathcal{O}\left(\frac{g^4}{\tilde{g}^4}\right),
$$

$$
g_{ZRW}^{(1)} = g_{ZRW}^{(2)} = g_{131} = 0, \qquad g_{ARR} = e,
$$

$$
g_{ZRR} = -\frac{g'^2}{\sqrt{g^2 + g'^2}},
$$

$$
g_{LZZ} = g_{LZ\gamma} = g_{RZZ} = g_{RZ\gamma} = 0. \tag{B8}
$$

The trilinear couplings of two vector fields with the Higgs boson, expressed in terms of M_Z, v and the Weinberg angle θ defined in Eq. (25) as well as a and δ defined in Eqs. (18) and (19), are given by

$$
g_{HZZ} = \frac{2}{v}M_Z^2(1-\delta)
$$
$$
= \frac{2}{v}M_Z^2\left\{1 - a\left[\frac{M_Z^4}{\tilde{g}^2 v^2 M_R^2}\left(3 + \cos(4\theta)\right) + \mathcal{O}\left(\frac{g^6}{\tilde{g}^6}\right)\right]\right\}, \tag{B9}
$$

$$
g_{HW^+W^-} = \frac{2}{v}M_W^2\left\{1 - a\left[\frac{M_Z^4}{\tilde{g}^2 v^2 M_R^2}\left(4\cos^4\theta\right) + \mathcal{O}\left(\frac{g^6}{\tilde{g}^6}\right)\right]\right\}
$$
$$
= \frac{2}{v}M_Z^2\cos^2\theta\left\{1 - \frac{M_Z^4}{\tilde{g}^2 v^2 M_R^2}\left(4a\cos^4\theta\right.\right.
$$
$$
\left.\left. - \sin(2\theta)\tan(2\theta)\right) + \mathcal{O}\left(\frac{g^6}{\tilde{g}^6}\right)\right\}, \tag{B10}
$$

$$g_{HL^0Z} = -a\frac{M_Z^3}{\tilde{g}v^2}4\cos^2\theta + \mathcal{O}\left(\frac{g^3}{\tilde{g}^3}\right)$$
$$= -\delta\frac{\tilde{g}M_R^2}{M_Z}\frac{4\cos^2\theta}{3+\cos(4\theta)} + \mathcal{O}\left(\frac{g^3}{\tilde{g}^3}\right), \qquad \text{(B11)}$$

$$g_{HR^0Z} = a\frac{M_Z^3}{\tilde{g}v^2}4\sin^2\theta + \mathcal{O}\left(\frac{g^3}{\tilde{g}^3}\right)$$
$$= \delta\frac{\tilde{g}M_R^2}{M_Z}\frac{4\sin^2\theta}{3+\cos(4\theta)} + \mathcal{O}\left(\frac{g^3}{\tilde{g}^3}\right), \qquad \text{(B12)}$$

$$g_{HL^+W^-} = -a\frac{M_Z^3}{\tilde{g}v^2}4\cos^3\theta + \mathcal{O}\left(\frac{g^3}{\tilde{g}^3}\right)$$
$$= -\delta\frac{\tilde{g}M_R^2}{M_Z}\frac{4\cos^3\theta}{3+\cos(4\theta)} + \mathcal{O}\left(\frac{g^3}{\tilde{g}^3}\right), \qquad \text{(B13)}$$

$$g_{HL^+L^-} = \frac{2M_R^2}{v}(1-a)\left[1 + \frac{4M_Z^2\cos^2\theta}{\tilde{g}^2v^2} + \mathcal{O}\left(\frac{g^4}{\tilde{g}^4}\right)\right]$$
$$= \frac{2M_R^2}{v}\left(1 - \delta\frac{\tilde{g}^2M_R^2v^2}{M_Z^4(\cos(4\theta)+3)}\right)$$
$$\times \left[1 + \frac{4M_Z^2\cos^2\theta}{\tilde{g}^2v^2} + \mathcal{O}\left(\frac{g^4}{\tilde{g}^4}\right)\right], \qquad \text{(B14)}$$

$$g_{HR^+R^-} = \frac{2M_R^2}{v}(1-a). \qquad \text{(B15)}$$

The couplings between fermions and the vector fields are

$$g_{R^0f}^{L/R} = \frac{g'^2}{\tilde{g}}\left(T_f^3\delta_L - \frac{g'^2}{g^2+g'^2}Q_f\right) + \mathcal{O}\left(\frac{g^2}{\tilde{g}^2}\right), \qquad \text{(B16)}$$

$$g_{L^0f}^{L/R} = -\frac{g^2}{\tilde{g}}\left(T_f^3\delta_L - \frac{g'^2}{g^2+g'^2}Q_f\right) + \mathcal{O}\left(\frac{g^2}{\tilde{g}^2}\right), \qquad \text{(B17)}$$

$$g_{L^\pm ud}^L = \frac{g^2}{\sqrt{2}\tilde{g}} + \mathcal{O}\left(\frac{g^2}{\tilde{g}^2}\right), \qquad \text{(B18)}$$

$$g_{R^\pm ud}^{L/R} = g_{L^\pm ud}^R = 0, \qquad \text{(B19)}$$

where $\delta_L = 1, 0$ for L and R, the left-handed and right-handed fermions, respectively.

APPENDIX C: DECAY WIDTHS

Below we give the partial widths of the heavy $\mathcal{R}$ resonances, see e.g., [57],

$$\Gamma(\mathcal{R} \to f\bar{f}) = \frac{m_{\mathcal{R}}N_c}{12\pi}\sqrt{1 - \frac{4m_f^2}{m_{\mathcal{R}}^2}}\left[(g_f^V)^2 + (g_f^A)^2\right.$$
$$\left. + \frac{m_f^2}{m_{\mathcal{R}}^2}(2(g_f^V)^2 - 4(g_f^A)^2)\right], \qquad \text{(C1)}$$

$$\Gamma(\mathcal{R} \to W^+W^-) = \frac{1}{192\pi}m_{\mathcal{R}}\left(\frac{m_{\mathcal{R}}}{M_W}\right)^4\left(1 - 4\frac{M_W^2}{m_{\mathcal{R}}^2}\right)^{1/2}$$
$$\times \left((g_{WW1}^{\mathcal{R}})^2\left[4\frac{M_W^2}{m_{\mathcal{R}}^2} - 4\frac{M_W^4}{m_{\mathcal{R}}^4} - 48\frac{M_W^6}{m_{\mathcal{R}}^6}\right]\right.$$
$$+ (g_{WW2}^{\mathcal{R}})^2\left[1 - 16\frac{M_W^4}{m_{\mathcal{R}}^4}\right]$$
$$+ g_{WW1}^{\mathcal{R}}g_{WW2}^{\mathcal{R}}\left[12\frac{M_W^2}{m_{\mathcal{R}}^2} - 48\frac{M_W^4}{m_{\mathcal{R}}^4}\right]$$
$$\left. + (g_{WW3}^{\mathcal{R}})^2\left[4\frac{M_W^2}{m_{\mathcal{R}}^2} - 32\frac{M_W^4}{m_{\mathcal{R}}^4} + 64\frac{M_W^6}{m_{\mathcal{R}}^6}\right]\right), \qquad \text{(C2)}$$

$$\Gamma(\mathcal{R} \to ZZ) = \frac{(g_{ZZ}^{\mathcal{R}})^2}{96\pi}m_{\mathcal{R}}\frac{m_{\mathcal{R}}^2}{M_Z^2}\left(1 - 4\frac{M_Z^2}{m_{\mathcal{R}}^2}\right)^{3/2}\left[1 - 6\frac{M_Z^2}{m_{\mathcal{R}}^2}\right], \qquad \text{(C3)}$$

$$\Gamma(\mathcal{R} \to Z\gamma) = \frac{(g_{Z\gamma}^{\mathcal{R}})^2}{96\pi}m_{\mathcal{R}}\frac{m_{\mathcal{R}}^2}{M_Z^2}\left(1 - \frac{M_Z^2}{m_{\mathcal{R}}^2}\right)^3, \qquad \text{(C4)}$$

$$\Gamma(\mathcal{R} \to ZH) = \frac{(g_{ZH}^{\mathcal{R}})^2}{192\pi M_Z^2}m_{\mathcal{R}}\sqrt{\lambda(1, x_Z, x_H)}$$
$$\times (\lambda(1, x_Z, x_H) + 12x_Z), \qquad \text{(C5)}$$

where $x_Z = (M_Z/m_{\mathcal{R}})^2$, $x_H = (m_H/m_{\mathcal{R}})^2$, and $\lambda(x, y, z) = x^2 + y^2 + z^2 - 2xy - 2yz - 2zx$.

APPENDIX D: OFF-DIAGONAL WIDTHS

The following is basically a summary of the basic effect from off-diagonal width. Loop corrections to the vector self-energy can be parametrized as

$$\Pi_{\mu\nu} = \Pi_T g_{\mu\nu} + \Pi_L p_\mu p_\nu. \qquad \text{(D1)}$$

The corrected vector-particles propagator can be written as

$$i\Delta_{\mu\nu} = \left(g_{\mu\nu} - \frac{p_\mu p_\nu}{p^2}\right)\frac{-i}{p^2 - M_0^2 + \Pi_T}$$
$$+ \frac{p_\mu p_\nu}{p^2}\frac{-i\xi}{p^2 - \xi(M_0^2 - \Pi_T - p^2\Pi_L)}. \qquad \text{(D2)}$$

Π_T defines the gauge independent pole mass and width while Π_L contributes to the gauge dependent pole and is negligible at the physical pole. Therefore we neglect Π_L and adopt the unitary gauge, $\xi \to \infty$. After diagonalization and renormalization, we get[9]

---

[9]Notice that the renormalization of fields and mass parameters allow us to fix the off-diagonal real part one-loop contribution to zero.

$$i\Delta_{\mu\nu} = \left(g_{\mu\nu} - \frac{p_\mu p_\nu}{p^2}\right)(-i)\Delta, \qquad \text{(D3)}$$

where, in the two-particles case,

$$i\Delta = \frac{i}{D}\begin{pmatrix} p^2 - m_2^2 + i\Sigma_{22} & -i\Sigma_{12} \\ -i\Sigma_{21} & p^2 - m_1^2 + i\Sigma_{11} \end{pmatrix}, \qquad \text{(D4)}$$

and $\Sigma_{ij} = \Im\Pi_{ij}$ for particle indexes $i, j = 1, 2$ and

$$D = (p^2 - m_1^2 + i\Sigma_{11})(p^2 - m_2^2 + i\Sigma_{22}) + \Sigma_{12}\Sigma_{21}. \qquad \text{(D5)}$$

APPENDIX E: FUTURE REACH

Our projected reach estimate is based on the search in the electron channel by the CMS experiment described in [19].

We assume a constant efficiency of 89% for both background and signal and apply the kinematic cuts:

$$|\eta(\ell^\pm)| < 2.5,$$
$$p_T(\ell^\pm) > 25 \text{ GeV}. \qquad \text{(E1)}$$

Signal.—The signal cross section, σ_S, is computed at LO and a mass dependent K factor is applied to account for QCD NNLO corrections. The K factors for resonance masses $M = 1$ TeV, 2 TeV, 3 TeV are 1.22, 1.16, and 1.16, respectively. We fix $a = 0$ for the projection and expect slightly weaker bounds for nonzero a.

Background.—The dominant DY background $pp \to Z/\gamma \to e^+e^-$ is computed at LO and the NNLO QCD and NLO EW corrections are incorporated through a mass dependent K factor. The k factors for $m(\ell\ell) = 1$ TeV,

2 TeV, 3 TeV are 1.07, 1.1, and 1.14, respectively. The sum of other background processes, $t\bar{t}$, tW, WW, WZ, ZZ, $\tau\tau$ and jets producing "fake" electrons have the same exponential falloff as a function of dilepton invariant mass as the DY for $m(\ell\ell) \gtrsim 200$ GeV. They can therefore be modeled as a number times the DY cross section. We take this number to be $r = 0.24$.

Statistics.—We look for a local excess in the mass window $M_R - 30$ GeV $< m(\ell\ell) < M_R + 150$, for each value of M_R. A Poisson distribution is assumed for the expected number of background events, N_B,

$$P(N; \mu) = \frac{\mu^N}{N!}e^{-\mu}, \qquad \text{(E2)}$$

with the predicted cross section times the integrated luminosity as the mean value,

$$\mu = \sigma_B L. \qquad \text{(E3)}$$

We denote the maximum number of events at 95% C.L., assuming the background only hypothesis, by N_{95},[10]

$$95\% = \sum_{N=0}^{N_{95}} \frac{\mu^N}{N!}e^{-\mu}. \qquad \text{(E4)}$$

Cross sections for which $\mu_S = \sigma_S L$, is larger than N_{95} are then considered excluded. The resulting exclusion limit presented in Fig. 22 is slightly stronger than our exclusion limit given in the upper left panel of Fig. 19. This is not surprising given the simplicity of the analysis.

---

[10]Fractional values of N_{95}, assuming uniform probability for each N, are necessary to be used for extremely small values of μ.

[1] T. Appelquist and F. Sannino, The physical spectrum of conformal SU(N) gauge theories, Phys. Rev. D **59**, 067702 (1999).

[2] T. Appelquist, P. S. Rodrigues da Silva, and F. Sannino, Enhanced global symmetries and the chiral phase transition, Phys. Rev. D **60**, 116007 (1999).

[3] R. Foadi, M. T. Frandsen, and F. Sannino, Constraining walking and custodial technicolor, Phys. Rev. D **77**, 097702 (2008).

[4] R. Casalbuoni, A. Deandrea, S. De Curtis, D. Dominici, F. Feruglio, R. Gatto, and M. Grazzini, Symmetries for vector and axial vector mesons, Phys. Lett. B **349**, 533 (1995).

[5] R. Casalbuoni, D. Dominici, A. Deandrea, R. Gatto, S. De Curtis, and M. Grazzini, Degenerate BESS model: The Possibility of a low-energy strong electroweak sector, Phys. Rev. D **53**, 5201 (1996).

[6] R. Casalbuoni, S. De Curtis, D. Dominici, and M. Grazzini, An extension of the electroweak model with decoupling at low energy, Phys. Lett. B **388**, 112 (1996).

[7] R. Casalbuoni, S. De Curtis, D. Dominici, and M. Grazzini, New vector bosons in the electroweak sector: A renormalizable model with decoupling, Phys. Rev. D **56**, 5731 (1997).

[8] S. De Curtis, D. Dolce, and D. Dominici, The scalar sector in an extended electroweak gauge symmetry model, Phys. Lett. B **579**, 140 (2004).

[9] A. E. Carcamo Hernandez and R. Torre, A "composite" scalar-vector system at the LHC, Nucl. Phys. **B841**, 188 (2010).

[10] A. Belyaev, R. Foadi, M. T. Frandsen, M. Järvinen, F. Sannino, and A. Pukhov, Technicolor walks at the LHC, Phys. Rev. D **79**, 035006 (2009).

[11] R. Contino, D. Marzocca, D. Pappadopulo, and R. Rattazzi, On the effect of resonances in composite Higgs phenomenology, J. High Energy Phys. 10 (2011) 081.

[12] D. Greco and Da Liu, Hunting composite vector resonances at the LHC: naturalness facing data, J. High Energy Phys. 12 (2014) 126.

[13] G. Brooijmans, R. Contino, B. Fuks, F. Moortgat, P. Richardson et al., Les Houches 2013: Physics at TeV colliders: New Physics Working Group Report, arXiv:1405.1617.

[14] K. Agashe, H. Davoudiasl, S. Gopalakrishna, T. Han, G.-Yu Huang, G. Perez, Z.-Guo Si, and A. Soni, LHC signals for warped electroweak neutral gauge bosons, Phys. Rev. D **76,** 115015 (2007).

[15] K. Agashe, S. Gopalakrishna, T. Han, G.-Yu Huang, and A. Soni, LHC signals for warped electroweak charged gauge bosons, Phys. Rev. D **80,** 075007 (2009).

[16] K. Agashe, A. Azatov, T. Han, Y. Li, Z.-Guo Si, and L. Zhu, LHC signals for coset electroweak gauge bosons in warped/composite PGB Higgs models, Phys. Rev. D **81,** 096002 (2010).

[17] D. Pappadopulo, A. Thamm, R. Torre, and A. Wulzer, Heavy vector triplets: Bridging theory and data, J. High Energy Phys. 09 (2014) 060.

[18] K. Hagiwara, R. D. Peccei, D. Zeppenfeld, and K. Hikasa, Probing the weak boson sector in $e^+e^- \to W^+W^-$, Nucl. Phys. **B282,** 253 (1987).

[19] CMS Collaboration, Technical Report No. CMS-PAS-EXO-12-061, CERN, Geneva, 2013.

[20] G. Aad et al. (ATLAS Collaboration), Search for high-mass dilepton resonances in pp collisions at $\sqrt{s} = 8$ TeV with the ATLAS detector, Phys. Rev. D **90,** 052005 (2014).

[21] G. Aad et al. (ATLAS Collaboration), Search for WZ resonances in the fully leptonic channel using pp collisions at $\sqrt{s} = 8$ TeV with the ATLAS detector, Phys. Lett. B **737,** 223 (2014).

[22] CMS Collaboration Technical Report No. CMS-PAS-EXO-12-025, CERN, Geneva, 2013.

[23] G. Aad et al. (ATLAS Collaboration), Search for new phenomena in the WW to $\ell\nu\ell'\nu'$ final state in pp collisions at $\sqrt{s} = 7$ TeV with the ATLAS detector, Phys. Lett. B **718,** 860 (2013).

[24] CMS Collaboration, Technical Report No. CMS-PAS-EXO-12-021, CERN, Geneva, 2013.

[25] S. Chatrchyan et al. (CMS Collaboration), Search for the standard model Higgs boson produced in association with a W or a Z boson and decaying to bottom quarks, Phys. Rev. D **89,** 012003 (2014).

[26] G. Aad et al. (ATLAS Collaboration), Search for the $b\bar{b}$ decay of the Standard Model Higgs boson in associated $(W/Z)H$ production with the ATLAS detector, J. High Energy Phys. 01 (2015) 069.

[27] CMS Collaboration, Technical Report No. CMS-PAS-EXO-12-060, CERN, Geneva, 2013.

[28] CMS Collaboration, Technical Report No. ATLAS-CONF-2014-017, CERN, Geneva, 2014.

[29] G. Aad et al. (ATLAS Collaboration), Search for resonant diboson production in the $\ell\ell q\bar{q}$ final state in pp collisions at $\sqrt{s} = 8$ TeV with the ATLAS detector, Eur. Phys. J. C **75,** 69 (2015).

[30] V. Khachatryan et al. (CMS Collaboration), Search for massive resonances decaying into pairs of boosted bosons in semi-leptonic final states at $\sqrt{s} = 8$ TeV, J. High Energy Phys. 08 (2014) 174.

[31] CMS Collaboration, Technical Report No. CMS-PAS-SMP-14-003, CERN, Geneva, 2014.

[32] S. Dittmaier et al. (LHC Higgs Cross Section Working Group), Handbook of LHC Higgs cross sections: 1. Inclusive observables, arXiv:1101.0593.

[33] Zhi-yong Duan, P. S. Rodrigues da Silva, and F. Sannino, Enhanced global symmetry constraints on epsilon terms, Nucl. Phys. **B592,** 371 (2001).

[34] R. Casalbuoni, S. De Curtis, and M. Redi, Signals of the degenerate BESS model at the LHC, Eur. Phys. J. C **18,** 65 (2000).

[35] R. Foadi, The unobservable axial-pion mixing in QCD and near-conformal dynamics, Eur. Phys. J. Plus **129,** 148 (2014).

[36] S. Chatrchyan et al. (CMS Collaboration), Searches for long-lived charged particles in pp collisions at $\sqrt{s} = 7$ and 8 TeV, J. High Energy Phys. 07 (2013) 122.

[37] R. Casalbuoni, S. De Curtis, D. Dominici, F. Feruglio, and R. Gatto, Vector and axial vector bound states from a strongly interacting electroweak sector, Int. J. Mod. Phys. A **04,** 1065 (1989).

[38] R. Barbieri, A. Pomarol, R. Rattazzi, and A. Strumia, Electroweak symmetry breaking after LEP-1 and LEP-2, Nucl. Phys. **B703,** 127 (2004).

[39] R. Foadi, M. T. Frandsen, T. A. Ryttov, and F. Sannino, Minimal walking technicolor: Setup for collider physics, Phys. Rev. D **76,** 055005 (2007).

[40] R. Casalbuoni, F. Coradeschi, S. De Curtis, and D. Dominici, A linear moose model with pairs of degenerate gauge boson triplets, Phys. Rev. D **77,** 095005 (2008).

[41] R. Foadi and F. Sannino, S and T parameters from a aight nonstandard Higgs versus near conformal dynamics, Phys. Rev. D **87,** 015008 (2013).

[42] M. Ciuchini, E. Franco, S. Mishima, and L. Silvestrini, Electroweak precision observables, new physics and the nature of a 126 GeV Higgs boson, J. High Energy Phys. 08 (2013) 106.

[43] M. Ciuchini, E. Franco, S. Mishima, M. Pierini, L. Reina et al., Update of the electroweak precision fit, interplay with Higgs-boson signal strengths and model-independent constraints on new physics, arXiv:1410.6940.

[44] ATLAS Collaboration, Technical Report No ATLAS-CONF-2014-009, CERN, Geneva, 2014.

[45] G. Altarelli and R. Barbieri, Vacuum polarization effects of new physics on electroweak processes, Phys. Lett. B **253,** 161 (1991).

[46] J. Alwall, M. Herquet, F. Maltoni, O. Mattelaer, and T. Stelzer, MADGRAPH 5: Going beyond, J. High Energy Phys. 06 (2011) 128.

[47] A. Alloul, N. D. Christensen, C. Degrande, C. Duhr, and B. Fuks, FeynRules 2.0—A complete toolbox for tree-level phenomenology, Comput. Phys. Commun. **185,** 2250 (2014).

[48] V. Khachatryan et al. (CMS Collaboration), Search for physics beyond the standard model in final states with a lepton and missing transverse energy in proton-proton collisions at $\sqrt{s} = 8$ TeV, Phys. Rev. D **91,** 092005 (2015).

[49] S. Chatrchyan *et al.* (CMS Collaboration), Search for narrow resonances in dilepton mass spectra in pp collisions at $\sqrt{s} = 7$ TeV, Phys. Lett. B **714**, 158 (2012).

[50] E. Accomando, D. Becciolini, A. Belyaev, S. Moretti, and C. Shepherd-Themistocleous, Z' at the LHC: Interference and finite width effects in Drell-Yan, J. High Energy Phys. 10 (2013) 153.

[51] G. Cacciapaglia, A. Deandrea, and S. De Curtis, Nearby resonances beyond the Breit-Wigner approximation, Phys. Lett. B **682**, 43 (2009).

[52] E. Accomando, D. Becciolini, S. De Curtis, D. Dominici, L. Fedeli, and C. Shepherd-Themistocleous, Interference effects in heavy W'-boson searches at the LHC, Phys. Rev. D **85**, 115017 (2012).

[53] G. Aad *et al.* (ATLAS Collaboration), Search for new particles in events with one lepton and missing transverse momentum in pp collisions at $\sqrt{s} = 8$ TeV with the ATLAS detector, J. High Energy Phys. 09 (2014) 037.

[54] M. Hoffmann, A. Kaminska, R. Nicolaidou, and S. Paganis, Probing compositeness with Higgs boson decays at the LHC, Eur. Phys. J. C **74**, 3181 (2014).

[55] A. R. Zerwekh, Associate Higgs and gauge boson production at hadron colliders in a model with vector resonances, Eur. Phys. J. C **46**, 791 (2006).

[56] V. Barger, P. Langacker, and H.-Sung Lee, Six-Lepton Z' Rresonance at the Large Hadron Collider, Phys. Rev. Lett. **103**, 251802 (2009).

[57] M. T. Frandsen, F. Kahlhoefer, A. Preston, S. Sarkar, and K. Schmidt-Hoberg, LHC and tevatron bounds on the dark matter direct detection cross-section for vector mediators, J. High Energy Phys. 07 (2012) 123.